

Towards the direct simulation of the quasi-biennial oscillation in a global storm-resolving model

Henning Franke^{1,2}, Marco A. Giorgetta¹

¹Max Planck Institute for Meteorology, Hamburg, Germany

²International Max Planck Research School on Earth System Modelling, Max Planck Institute for
Meteorology, Hamburg, Germany

Key Points:

- The ability of the general circulation model ICON, which explicitly simulates deep convection and gravity waves, to simulate a QBO is tested
- ICON simulates a reasonable downward propagation and momentum balance of QBO-like jets in the upper QBO domain in the first simulation year
- The simulated QBO-like jets stall in the lowermost stratosphere due to a lack of planetary wave forcing resulting from a lack of CCEWs

Corresponding author: Henning Franke, henning.franke@mpimet.mpg.de

Abstract

This study presents the first attempt to directly simulate a full cycle of the quasi-biennial oscillation (QBO) in a global storm-resolving model (GSRM) that explicitly simulates deep convection and gravity waves instead of parameterizing them. Using the Icosahedral Nonhydrostatic (ICON) model with horizontal and vertical resolutions of about 5 km and 400 m, respectively, we show that an untuned state-of-the-art global storm-resolving model is already on the verge of simulating a QBO-like oscillation of the zonal wind in the tropical stratosphere for the right reasons. ICON shows overall good fidelity in simulating the QBO momentum budget and the downward propagation of the QBO jets in the upper QBO domain (25 km–35 km). In the lowermost stratosphere, however, ICON does not simulate the downward propagation of the QBO jets to the tropopause. This is the result of a pronounced lack of QBO wave forcing, mainly on planetary scales. We show that the lack of planetary-scale wave forcing in the lowermost stratosphere is caused by an underestimation of the planetary-scale wave momentum flux entering the stratosphere, which is too weak by 20%–40%. We attribute this lack of planetary-scale wave momentum flux to a substantial lack of convectively coupled equatorial waves in the tropical troposphere. Therefore, we conclude that in the present global storm-resolving model, simulating a realistic spatio-temporal variability of tropical deep convection, in particular convectively coupled equatorial waves, is currently the main roadblock towards simulating a reasonable QBO.

Plain Language Summary

The quasi-biennial oscillation (QBO) is a wind system located in the equatorial stratosphere between ~17 km and ~35 km and consists of westerly and easterly wind jets that alternately propagate downward with time. The QBO has been shown to influence surface weather, so it is important to simulate the QBO realistically in the computer models typically used for climate research. However, these models often struggle to simulate a realistic QBO because they represent the processes leading up to the QBO, i.e. tropical rain showers and short atmospheric waves excited by these rain showers, only empirically through so-called parameterizations. In this study, we attempt for the first time to simulate the QBO in a model that directly represents these processes through an ultra-fine grid. We find that our model maintains QBO-like stratospheric winds throughout the simulation, and in the central stratosphere, the model simulates the characteristics of the QBO reasonably well for the right reasons. However, in the lowermost stratosphere, the simulated QBO is not realistic and does not move downward with time as observed due to a misrepresentation of long waves in the tropical atmosphere. These results will guide future model development to improve the model’s representation of the QBO.

1 Introduction

The quasi-biennial oscillation (QBO) is a more or less regular downward propagating oscillation of the zonal wind in the tropical stratosphere, driven by the breaking and dissipation of upwardly propagating tropical waves (Baldwin et al., 2001). The wave spectrum that drives the QBO ranges from large-scale planetary waves to small-scale gravity waves (GWs), and the vast majority of these waves are generated by tropical deep convection (e.g., Holton, 1972; Fritts & Alexander, 2003). However, deep convection and a substantial part of the GW spectrum are not resolved by conventional general circulation models (GCMs), which typically employ horizontal grid spacings of $\mathcal{O}(100\text{ km})$. Therefore, deep convection and GWs are usually parameterized in these models, which leads to considerable uncertainties in the simulated QBO (Bushell et al., 2020). In this study, we present the first attempt to overcome this uncertainty by a direct simulation of a full QBO cycle in a GCM that no longer parameterizes deep convection and GWs but instead explicitly simulates both processes — and thus the entire QBO forcing.

64 Successfully modeling the QBO in a realistic manner has ever since posed a ma-
 65 jor challenge to conventional three-dimensional GCMs, and the fidelity of simulated QBOs
 66 in such models has increased only slightly over the last two decades (Schenzinger et al.,
 67 2017; Richter, Anstey, et al., 2020). This motivated the recent model intercomparison
 68 project Quasi-Biennial Oscillation initiative (QBOi), which aimed to asses the status quo
 69 of the ability of the latest GCMs to simulate a QBO and to identify possible avenues for
 70 improvement (Butchart et al., 2018). As one of the main results of QBOi, it was shown
 71 that the partitioning of the QBO wave forcing between resolved and parameterized waves
 72 is highly model-dependent, with the contribution of the parameterized GWs varying be-
 73 tween 40% and 80% (Bushell et al., 2020). On the one hand, this large intermodel spread
 74 can be directly attributed to the inherent uncertainty of the GW parameterizations them-
 75 selves, which results from the necessary simplifying assumptions in their formulation. These
 76 simplifications include that most GW parameterizations allow only for instantaneous and
 77 vertical GW propagation, often do not account for GW intermittency and secondary gen-
 78 eration, and usually prescribe a fixed GW source spectrum (Plougonven et al., 2020; Achatz
 79 et al., 2023). The prescribed GW source spectrum is still poorly constrained by obser-
 80 vations and thus varies widely between different models (Alexander et al., 2010). On the
 81 other hand, the uncertainty in the relative contribution of resolved and parameterized
 82 waves to driving the QBO is a consequence of the fact that GW parameterizations are
 83 often used to optimize the simulated QBO to achieve a somewhat realistic QBO period
 84 and amplitude (e.g., Garfinkel et al., 2022).

85 In part, the tuning becomes necessary to compensate for biases in the resolved wave
 86 forcing of the QBO. These biases often arise from the parameterization of deep convec-
 87 tion, which affects the representation of convectively coupled equatorial waves (CCEWs)
 88 (e.g., Lin et al., 2008; Straub et al., 2010; Frierson et al., 2011). Since CCEWs are closely
 89 related to stratospheric equatorial waves (SEWs), the details of the parameterization of
 90 deep convection can affect the resolved wave momentum fluxes in the lower stratosphere,
 91 which contribute to driving the QBO (Ricciardulli & Garcia, 2000; Horinouchi et al., 2003).
 92 Furthermore, the parameterization of deep convection directly or indirectly provides the
 93 input fields that are used to estimate the wave sources of interactive GW parameteri-
 94 zations (e.g., Beres et al., 2004; Richter et al., 2010; Bushell et al., 2015), thereby influ-
 95 encing the parameterized GW forcing of the QBO.

96 Obviously, the uncertainties associated with the parameterizations of deep convec-
 97 tion and GWs lead to substantial uncertainty in the overall QBO momentum budget.
 98 This severely limits our current understanding of the details of the QBO forcing. More-
 99 over, the GW parameterizations in many GCMs are overtuned toward a realistic rep-
 100 resentation of the present-day QBO, which prevents insight into out-of-sample conditions,
 101 as demonstrated for the question of how the QBO may change due to global warming
 102 (Schirber et al., 2015; Richter, Butchart, et al., 2020). Despite recent progress in the de-
 103 velopment of more sophisticated GW parameterizations (e.g., Bölöni et al., 2021; Y.-H. Kim
 104 et al., 2021), it is questionable whether the current approach to modeling the QBO will
 105 allow for fundamental new insights in the foreseeable future.

106 As a starting point to overcome this parameterization deadlock, Giorgetta et al.
 107 (2022) presented the first direct simulation of QBO jets over a short period of 48 days
 108 in a very high resolution GCM (~ 5 km horizontal, ~ 400 m vertical) that no longer em-
 109 ploys a parameterization of deep convection and GWs. This type of GCMs is commonly
 110 referred to as global storm-resolving models (GSRMs) (e.g., Satoh et al., 2019; Stevens
 111 et al., 2019). GSRMs offer substantial potential for reducing the long-standing uncer-
 112 tainty in modeling the QBO. However, current GSRMs mostly employ horizontal grid
 113 spacings between $\mathcal{O}(1$ km) and $\mathcal{O}(10$ km). These grid spacings are often referred to as
 114 the "convective gray zone" because they partially but not fully resolve deep convection,
 115 and thus neither traditional parameterizations of deep convection nor its explicit treat-
 116 ment work satisfactorily (e.g., Prein et al., 2015; Tomassini et al., 2023). As shown by

117 Polichtchouk et al. (2021), these problems in representing deep convection also affect the
 118 details of the simulated tropical GW spectrum, i.e. the partitioning of the resolved grav-
 119 ity wave momentum flux (GWMF) with respect to horizontal wavelength. They suggest
 120 that even at a horizontal grid spacing of less than 5 km, a scale-aware parameterization
 121 of deep convection may be necessary to accurately simulate the resolved GWMF.

122 However, it is currently unclear whether this fidelity in representing the details of
 123 the GW spectrum is really necessary for the simulation of a realistic QBO, or whether
 124 major aspects of the QBO can be already well captured in a GSRM operating in the gray
 125 zone. This question cannot be answered by the short simulation of Giorgetta et al. (2022),
 126 although they have shown that a state-of-the-art GSRM is in principle capable of simu-
 127 lating a reasonable wave-driven downward propagation of the QBO jets over a period
 128 of 48 days. Such short simulations can only work as a first proof of concept and allow
 129 for specific process studies, as demonstrated by Franke et al. (2023), who showed that
 130 the QBO is likely to become faster and stronger under global warming based on warming-
 131 induced changes of the QBO gravity wave forcing. However, such short studies do not
 132 allow for a systematic evaluation of the QBO and its forcing, which requires the simu-
 133 lation of at least one full QBO cycle.

134 This situation motivates the present study, which aims at the first direct simula-
 135 tion of a full QBO cycle in a GSRM which neither applies a parameterization of deep
 136 convection nor GWs. The simulation was performed by the global storm-resolving Icosa-
 137 hedral Nonhydrostatic (ICON) model with a horizontal grid spacing of about 5 km and
 138 a vertical grid spacing between 350 m and 560 m in the stratosphere. As this is the first
 139 simulation of its kind over such a long period, we certainly do not expect the model to
 140 simulate a QBO that is already close to reality. Rather, we want to find out whether a
 141 GSRM in the chosen configuration is able to capture the basic characteristics and dy-
 142 namics of the QBO and which aspects need further improvement. In doing so, we aim
 143 to provide a benchmark simulation to guide future model development. More specifically,
 144 we will address the following research questions:

- 145 1. *Is the state-of-the-art GSRM ICON in the present configuration capable of directly*
 146 *simulating a full cycle of the QBO in a reasonable way? Which aspects of the QBO*
 147 *are well captured and which are not?*
- 148 2. *Why does the model simulate the QBO the way it does?*
 149 *If the QBO is reasonably simulated, how is it forced in the simulation? Is it rea-*
 150 *sonable for the right reasons, or is it the product of compensating errors?*
 151 *If the QBO is not reasonably simulated, what are the sources of QBO biases? Are*
 152 *QBO biases caused by biases in other aspects of the simulation?*

153 2 Methods

154 2.1 Global storm-resolving ICON simulation

155 We conducted a two-year-long global storm-resolving simulation with the non-hydrostatic
 156 GSRM ICON in an atmosphere-only setup (Giorgetta et al., 2018). Following the sci-
 157 entific rationale of our study, this simulation employs neither a parameterization of deep
 158 convection nor a parameterization of orographic and non-orographic GWs. Instead, the
 159 horizontal and vertical resolution allows for an explicit representation of these processes.
 160 Horizontally, the simulation uses the R2B9 grid, which has an equivalent grid spacing
 161 of ~ 4.9 km (see Giorgetta et al., 2018, Tab. 1), and vertically it uses a grid with 191 lev-
 162 els up to an altitude of 83 km, resulting in a vertical grid spacing of ~ 350 m in the tropopause
 163 region and ~ 560 m in the stratopause region (see Giorgetta et al., 2022, Fig. 1). To en-
 164 sure the numerical stability of the model, we performed the simulation with a timestep
 165 of 30 s, which was further divided into 8 dynamics substeps. In contrast, (Giorgetta et
 166 al., 2022) used a timestep of 40 s and 5 dynamics substeps, which proved to be not sta-

167 ble enough for longer simulations. Details on the dynamical substepping can be found
 168 in Zängl et al. (2015). Since this storm-resolving model setup is computationally very
 169 demanding, we performed the simulation with the graphics processing unit (GPU)-enabled
 170 version of ICON (Giorgetta et al., 2022).

171 The storm-resolving configuration of ICON retains parameterizations for only three
 172 remaining processes: radiation, cloud microphysics, and turbulent vertical diffusion. For
 173 radiation, the GPU-enabled ICON employs the RTE+RRTMGP scheme (Pincus et al.,
 174 2019). Cloud microphysics is parameterized using a one-moment "graupel" microphysics
 175 scheme (Baldauf et al., 2011; Doms et al., 2021). The vertical diffusion of heat, momen-
 176 tum, and tracers is parameterized using a total turbulent energy scheme (Mauritsen et
 177 al., 2007; Pithan et al., 2015). This scheme represents the size of the largest turbulent
 178 eddies by calculating a turbulent length scale l , which by default is capped at $l_{\max} =$
 179 150 m outside the boundary layer (Pithan et al., 2015). In our simulation, we reduced
 180 l_{\max} to 50 m because $l_{\max} = 150$ m was found to lead to unreasonably strong vertical
 181 diffusion. For details on the parameterizations, please refer to Giorgetta et al. (2018) and
 182 Giorgetta et al. (2022).

183 In ICON, explicit horizontal diffusion is employed as a second-order Smagorinsky
 184 diffusion acting on potential temperature and horizontal velocity combined with a fourth-
 185 order background diffusion acting on horizontal velocity only with an e -folding time of
 186 1080 s. In addition, ICON employs a fourth-order divergence damping acting on three-
 187 dimensional divergence in order to ensure numerical stability. To avoid the unphysical
 188 reflection of waves at the top of the model, ICON employs a Rayleigh damping acting
 189 on the vertical velocity above 50 km (Klemp et al., 2008). Details on the formulation of
 190 the diffusion and damping acting in ICON can be found in Zängl et al. (2015).

191 The simulation itself was set up as a two-year-long time slice experiment initial-
 192 ized from the operational analysis of the Integrated Forecasting System of the European
 193 Centre for Medium-Range Weather Forecasts (ECMWF) on April 1, 2004 at 00:00:00 UTC.
 194 The boundary conditions closely follow the experimental protocol of the QBOi Exper-
 195 iment 2 (Butchart et al., 2018). Accordingly, the sea surface temperature (SST) and sea
 196 ice concentration (SIC) have been prescribed as a repeating annual cycle of the 1988–
 197 2007 monthly means from the corresponding Coupled Model Intercomparison Project
 198 phase 6 (CMIP6) input datasets (Durack & Taylor, 2019). The concentrations of car-
 199 bon dioxide (CO_2) and other radiatively active trace gases except ozone (O_3) were also
 200 set to their 1988–2007 mean values from the CMIP6 input dataset (Meinshausen et al.,
 201 2017), resulting in a CO_2 concentration of 365.59 ppm. The O_3 concentration is mod-
 202 eled interactively using the linearized ozone scheme of Cariolle and Teysse re (2007). Tro-
 203 pospheric aerosols are prescribed with their 2002 monthly means from the Max Planck
 204 Institute aerosol climatology (MAC; Kinne et al., 2013), and the solar forcing is also pre-
 205 scribed with its 2002 monthly means. The year 2002 was chosen based on the QBOi ex-
 206 perimental protocol (Butchart et al., 2018).

207 The simulation is analyzed based on three-hourly instantaneous output of atmo-
 208 spheric state variables and three-hourly averaged output of tendencies and fluxes. The
 209 output has been interpolated from the native triangular R2B9 grid to a regular n256 Gaus-
 210 sian grid, which has a grid spacing of ~ 39 km at the equator, using a distance-weighted
 211 remapping of the 13 nearest neighbors. The three-dimensional output fields were then
 212 further interpolated vertically from the native terrain-following hybrid sigma height co-
 213 ordinate to geometric height levels corresponding to the sigma height levels over ocean.
 214 Since the transition from terrain-following coordinate surfaces to flat coordinate surfaces
 215 occurs at an altitude of 22.5 km, the target height levels of the vertical interpolation are
 216 identical to the model levels above this altitude.

217

2.2 Reference datasets

218

219

To evaluate the simulated QBO, its zonal momentum budget, and the equatorial wave field, we compare the simulation to observationally constrained reference datasets.

220

2.2.1 ERA5 reanalysis

221

222

223

224

225

226

As a reference for the QBO and its zonal momentum budget, we use the ECMWF Reanalysis v5 (ERA5; Hersbach et al., 2020). We use only one reanalysis dataset as a reference because the representation of the QBO is very similar in different recent state-of-the-art reanalyses (SPARC, 2022, Chp. 9). The representation of the QBO in ERA5 itself has been investigated in detail by Pahlavan, Fu, et al. (2021); Pahlavan, Wallace, et al. (2021).

227

228

229

230

231

232

233

234

235

ERA5 has a spectral truncation of T639, corresponding to an n320 Gaussian grid, which has a grid spacing of ~ 31 km, and 137 hybrid sigma pressure levels up to 1 hPa. The three wind components, temperature, and the surface geopotential are provided on the original T639 spectral grid, while tracer and two-dimensional surface fields are provided on a reduced n320 Gaussian grid (Hersbach et al., 2018b, 2018a). Thus, in a first step, we interpolated the raw ERA5 data to the same regular n256 Gaussian grid as the ICON output using a distance-weighted remapping of the four nearest neighbours. We then interpolate the ERA5 data to the 191 geometric height levels of the postprocessed ICON output.

236

237

238

239

240

Please note that we used ERA5.1 instead of ERA5 for the period 2000–2006. This is due to the fact that ERA5 has a pronounced stratospheric cold bias during these years due to incorrect data assimilation, which has been fixed in ERA5.1 (Simmons et al., 2020). When we refer to ERA5 throughout this manuscript, we implicitly mean ERA5.1 during the years 2000–2006.

241

2.2.2 IMERG precipitation observations

242

243

244

245

246

247

248

249

As an additional reference dataset for tropical precipitation, we use a satellite-based observational product, the Integrated Multi-satellite Retrievals for the Global Precipitation Measurement (IMERG) for the period April 1, 2004–March 31, 2006 (Huffman et al., 2022). IMERG provides the half-hourly mean precipitation rate with a spatial resolution of $0.1^\circ \times 0.1^\circ$. We resampled the data to three-hourly mean precipitation rates to match the temporal resolution of the ICON output. Afterwards, we interpolated the data to the same regular n256 Gaussian grid as the ICON output, using a distance-weighted average remapping of the four nearest neighbours.

250

2.3 Diagnostics

251

2.3.1 Equatorial wave spectra

252

253

254

We investigate the equatorial wave field by means of spectral analysis in longitude λ and time t . The two-dimensional power spectrum P_x of a quantity $x(\lambda, t)$ with respect to zonal wavenumber k and frequency ω is calculated as

$$P_x(k, \omega) = \frac{1}{N_\lambda^2 N_t^2} \mathcal{F}_x(k, \omega) \tilde{\mathcal{F}}_x(k, \omega), \quad (1)$$

255

256

257

where \mathcal{F}_x is the complex Fourier transform of x , $\tilde{\mathcal{F}}_x$ is its complex conjugate, N_λ denotes the number of grid points in longitude, and N_t denotes the number of samples in time. The chosen normalization of $P_x(k, \omega)$ satisfies Parseval's theorem as

$$\frac{1}{N_\lambda N_t} \sum_{i=1}^{N_\lambda} \sum_{j=1}^{N_t} |x_{i,j}^2| = \sum_{k=-N_\lambda/2}^{N_\lambda/2} \sum_{\omega=-N_t/2}^{N_t/2} P_x(k, \omega). \quad (2)$$

258 Analogously, we define the cospectrum of two quantities $x(\lambda, t)$ and $y(\lambda, t)$ as

$$P_{xy}(k, \omega) = \frac{1}{N_\lambda^2 N_t^2} \Re \left(\mathcal{F}_x(k, \omega) \tilde{\mathcal{F}}_y(k, \omega) \right), \quad (3)$$

259 where \Re denotes the real part.

260 To diagnose CCEWs, we follow the methodology of Wheeler and Kiladis (1999) and
 261 split a quantity $x(\lambda, \phi, t)$, which depends on latitude ϕ into its symmetric and antisym-
 262 metric component with respect to the equator, $x_{\text{sym}}(\lambda, \phi, t)$ and $x_{\text{asym}}(\lambda, \phi, t)$, respec-
 263 tively:

$$\begin{aligned} x_{\text{sym}}(\lambda, \phi, t) &= \frac{x(\lambda, \phi, t) + x(\lambda, -\phi, t)}{2} \\ x_{\text{asym}}(\lambda, \phi, t) &= \frac{x(\lambda, \phi, t) - x(\lambda, -\phi, t)}{2}. \end{aligned} \quad (4)$$

264 We then compute the zonal wavenumber-frequency spectra of $x_{\text{sym}}(\lambda, \phi, t)$ and $x_{\text{asym}}(\lambda, \phi, t)$
 265 as described in Eq. 1 and normalize them by a smoothed background spectrum.

2.3.2 QBO momentum budget

266 To understand what processes drive the QBO in the ICON simulation, we diag-
 267 nose the QBO zonal momentum budget in the transformed Eulerian mean (TEM) frame-
 268 work (Andrews & McIntyre, 1976). The TEM framework allows for a clear separation
 269 between the different forcing processes of the QBO. We calculate the TEM zonal mo-
 270 mentum budget based on the hydrostatic primitive equations in geometric height coor-
 271 dinates (Hardiman et al., 2010):
 272

$$\bar{u}_{,t} = \bar{v}^* \left(f - \frac{(\bar{u} \cos \phi)_{,\phi}}{A \cos \phi} \right) - \bar{w}^* \bar{u}_{,z} + \frac{\nabla \cdot \mathbf{F}}{\bar{\rho} a \cos \phi} + \bar{X}. \quad (5)$$

273 Here, u denotes the zonal wind, f denotes the Coriolis parameter, ρ denotes the air den-
 274 sity, a denotes Earth's mean radius, which we set to $a = 6371$ km, ϕ denotes the lati-
 275 tude, v^* and w^* denote the meridional and vertical residual velocity, respectively, and
 276 \mathbf{F} denotes the Eliassen-Palm (EP) flux. Furthermore, an overbar represents the zonal
 277 mean, and the subscripts $(, t)$, $(, \phi)$, and $(, z)$ denote the partial derivatives with respect
 278 to time, latitude, and altitude, respectively.

279 In Eq. 5, the first and second term on the right-hand-side represent the accelera-
 280 tion of \bar{u} by the meridional and vertical residual advection of zonal mean axial angular
 281 momentum per unit mass, respectively. The third term on the right-hand-side of Eq. 5
 282 represents the wave forcing of \bar{u} which is resolved by the analysis grid, and $\nabla \cdot \mathbf{F}$ is given
 283 by

$$\nabla \cdot \mathbf{F} = \frac{(\cos \phi F^{(\phi)})_{,\phi}}{a \cos \phi} + F_{,z}^{(z)}, \quad (6)$$

284 where $F^{(\phi)}$ and $F^{(z)}$ denote the meridional and vertical component of \mathbf{F} , respectively.
 285 They are given by

$$\begin{aligned} F^{(\phi)} &\equiv -a \cos \phi \overline{(\rho v)' u'} + \psi \bar{u}_{,z} \\ F^{(z)} &\equiv -a \cos \phi \overline{(\rho w)' u'} - \psi \left(\frac{(\bar{u} \cos \phi)_{,\phi}}{A \cos \phi} - f \right). \end{aligned} \quad (7)$$

286 Here, a prime represents the deviation from the zonal mean, and ψ denotes the "differ-
 287 ence stream function" (cf. Hardiman et al., 2010) and is defined as

$$\psi \equiv \frac{a \cos \phi}{|\nabla \theta|^2} \left(\overline{(\rho v)' \theta'_{,z}} - \overline{(\rho w)' \theta'_{,\phi}} \frac{\bar{\theta}_{,\phi}}{a} \right), \quad (8)$$

288 where θ denotes the potential temperature. The fourth term on the right-hand-side of
 289 Eq. 5, \bar{X} , represents the residuum which remains when subtracting the previous three
 290 terms from the actual zonal wind tendency simulated by ICON. This means that \bar{X} con-
 291 tains all tendencies from processes not resolved by the TEM analysis, including the pa-
 292 rameterized tendency from vertical diffusion and diffusive tendencies from the dynam-
 293 ical core itself.

294 Following Horinouchi et al. (2003), we also calculate spectra of \mathbf{F} as a function of
 295 zonal wavenumber k and frequency ω :

$$\begin{aligned} F^{(\phi)}(k, \omega) &\equiv -a \cos\phi P_{(\rho v)'u'}(k, \omega) + \psi(k, \omega) \bar{u}_{,z} \\ F^{(z)}(k, \omega) &\equiv -a \cos\phi P_{(\rho w)'u'}(k, \omega) - \psi(k, \omega) \left(\frac{(\bar{u} \cos\phi)_{,\phi}}{A \cos\phi} - f \right) \end{aligned} \quad (9)$$

296 with

$$\psi(k, \omega) \equiv \frac{a \cos\phi}{|\nabla\theta|^2} \left(P_{(\rho v)'\theta'}(k, \omega) \bar{\theta}_{,z} - P_{(\rho w)'\theta'}(k, \omega) \frac{\bar{\theta}_{,\phi}}{a} \right). \quad (10)$$

297 Here, the cospectra $P_{(\rho v)'u'}$ and $P_{(\rho w)'u'}$ as well as $P_{(\rho v)'\theta'}$ and $P_{(\rho w)'\theta'}$ are calculated based
 298 on Eq. 3. For both ICON and ECMWF Reanalysis v5 (ERA5), we compute the TEM
 299 diagnostics based on the postprocessed data on the n256 Gaussian grid with 191 geo-
 300 metric height levels. This procedure follows the recommendations of Hardiman et al. (2010)
 301 for comparing TEM diagnostics between datasets on different native grids. It should be
 302 noted that the vertical remapping of the ERA5 data prior to the calculation of the TEM
 303 diagnostics can result in artefacts in the calculates wave forcing. However, we found this
 304 effect to be negligible.

305 **3 General structure of the QBO-like oscillation in the ICON simula-** 306 **tion**

307 Figure 1a shows the time evolution of the stratospheric 5° S–5° N mean zonal wind
 308 in the ICON simulation. Throughout the entire simulation, ICON sustains a QBO-like
 309 zonal wind structure of easterly and westerly wind jets alternating with altitude. The
 310 easterly shear zone (i.e., a change of winds from westerly to easterly with altitude), which
 311 is initially located between ~30 km and ~38 km, shows a clear downward propagation
 312 during the first year of the simulation. However, the downward propagation of the east-
 313 erly shear zone stops in the second year of the simulation, and the westerly shear zone,
 314 which is initially located between 18 km and 25 km, does not propagate downward at all.
 315 As a result, the westerly jet stalls and does not dissipate within the simulated period of
 316 two years, which means that ICON does not simulate a closed cycle of the QBO. Nev-
 317 ertheless, from now on we will refer to the spatio-temporal structure of the zonal wind
 318 in the equatorial stratosphere in the ICON simulation — as seen in Figure 1a — as the
 319 *ICON-QBO*.

320 In the following, we compare the ICON-QBO with selected individual QBO cycles
 321 in the ERA5 reanalysis during the years 1980–2015. This period has boundary condi-
 322 tions reasonably close to those of the ICON simulation, and it is free of QBO disruptions
 323 such as those observed in 2015/16 and 2019/20 (see Osprey et al., 2016; Anstey et al.,
 324 2021). To select reasonable individual QBO cycles for comparison, we first determine those
 325 years in which the QBO in March and April was in a phase comparable to that of March
 326 and April 2004 because we initialized the ICON simulation on April 01, 2004. The ap-
 327 plied criterion for this subsampling is a change of the monthly mean 5° S–5° N mean zonal
 328 wind at one of the four levels between 21 km and 22.5 km (i.e., 22.432 km, 22.051 km, 21.672 km,
 329 21.296 km) from easterly in March to westerly in April. This criterion is fulfilled by six
 330 years (1985, 1990, 1997, 2004, 2008, and 2013), which we will hereafter refer to as the
 331 *ERA5-QBO-ensemble*.

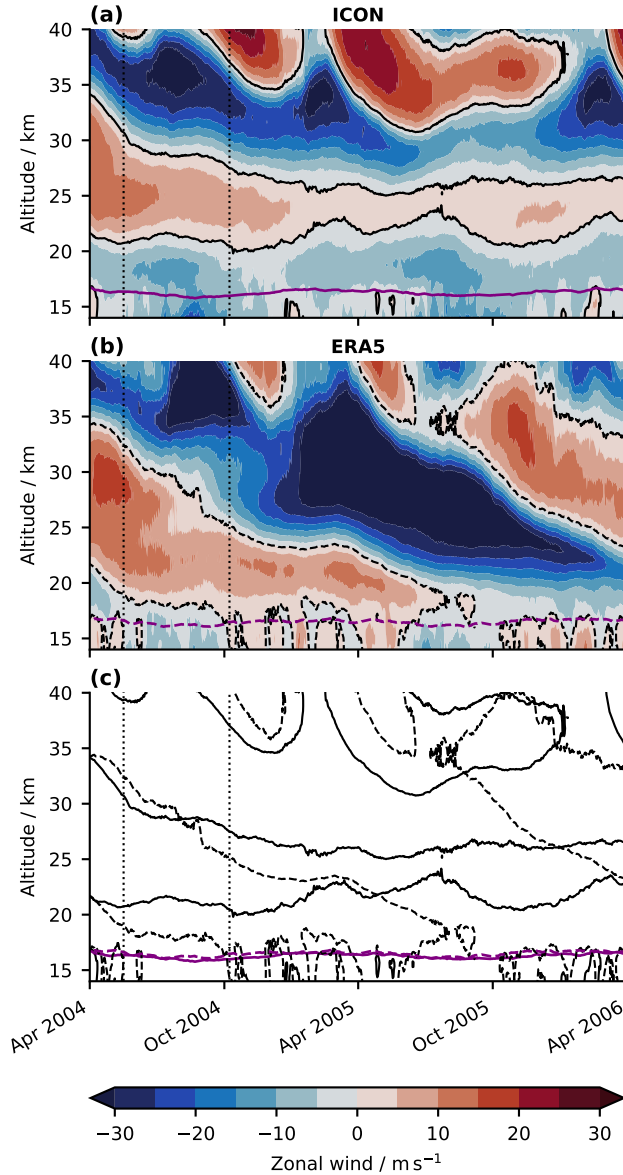


Figure 1. Time-altitude cross section of the 5°S – 5°N mean zonal wind for (a) the ICON simulation and (b) the ERA5 reanalysis during April 1, 2004–March 31, 2006. The (a) solid and (b) dashed black contour lines mark the 0 m s^{-1} -isotach. The (a) solid and (b) dashed purple contour lines mark the 370 K-isentrope, which serves as a proxy for the tropopause altitude. Panel (c) shows the 0 m s^{-1} -isotachs and 370 K-isentropes of panels (a) and (b) to allow a direct comparison between ICON and ERA5. The vertical dotted black lines in all panels mark the beginning and end of the period used to compare the zonal momentum budgets of the 5°S – 5°N mean zonal wind in ICON and ERA5 (see Sec. 4.2).

332 In Figure 2, we compare the time evolution of the 5°S – 5°N mean zonal wind be-
 333 tween the ICON simulation and the ERA5-QBO-ensemble. The basic spatio-temporal
 334 structure of the ICON-QBO is approximately within the cycle-to-cycle variability of the
 335 ERA5-QBO-ensemble in the first year of the simulation (Fig. 2a). During this period,
 336 ICON simulates an overall reasonable downward propagation of that 0 m s^{-1} -isotach, which

337 is initially located at ~ 34 km, at a rate comparable to that of individual cycles in the
 338 ERA5-QBO-ensemble. This also applies to the zonal wind jets associated with the semi-
 339 annual oscillation (SAO) between 35 km and 40 km. In the lowermost stratosphere, the
 340 comparison between the ICON-QBO and the ERA5-QBO-ensemble reveals the unreal-
 341 istic lack of downward propagation of the westerly jet of the ICON-QBO right from the
 342 beginning of the simulation, which was already identified in Figure 1a. During the sec-
 343 ond year of the simulation, the spatio-temporal structure of the ICON-QBO is no longer
 344 consistent with the ERA5-QBO-ensemble throughout the entire stratosphere.

345 Figure 2b further shows that the jets of the ICON-QBO are weaker than those of
 346 the ERA5-QBO-ensemble in both the lower and upper QBO domain throughout the en-
 347 tire simulation. The vertical structure of ICON-QBO is not consistent with the ERA5-
 348 QBO-ensemble right from the beginning of the simulation. In addition, Figure 2b clearly
 349 shows that the ICON-QBO is trapped at the end of the simulation due to its lack of down-
 350 ward propagation.

351 Although the six individual QBO cycles of the ERA5-QBO-ensemble do not pro-
 352 vide a statistically significant reference sample, we conclude at this point that the ICON-
 353 QBO is not realistic. It suffers from a pronounced lack of downward propagation, which
 354 begins in the lowermost stratosphere right at the beginning of the simulation and ap-
 355 pears to spread upward subsequently. During the last months of the simulation, basi-
 356 cally all zonal wind jets of the ICON-QBO below ~ 30 km do no longer propagate down-
 357 ward.

358 To further highlight the shortcomings of the ICON-QBO in more detail, we com-
 359 pare it to one specific QBO cycle of the ERA5-QBO-ensemble, which is the cycle begin-
 360 ning on April 1, 2004 (Fig. 1b). The comparison with a single QBO cycle is justified be-
 361 cause all individual QBO cycles of the ERA5-QBO-ensemble agree reasonably well among
 362 each other, except for the cycle affected by the eruption of Mt. Pinatubo (Fig. 2b). From
 363 now on, we will refer to the ERA5 QBO cycle beginning on April 1, 2004 as the *ERA5-
 364 QBO*. The comparison between the ICON-QBO and the ERA5-QBO basically confirms
 365 the previous results, and in particular highlights that the ICON-QBO has too weak jets
 366 below 30 km, especially during the second year of the simulation. During this period, the
 367 jets of the ICON-QBO also have a much smaller vertical extent than those of the ERA5-
 368 QBO. In addition, the vertical gradient of the zonal wind within the shear zones of the
 369 ICON-QBO is much weaker than in those of the ERA5-QBO, at least below 30 km.

370 Figure 1 also shows that the altitude of the tropopause in the ICON simulation and
 371 the ERA5 reanalysis is approximately identical. Thus, we already rule out a too high
 372 tropopause in ICON as a root cause for the lack of downward propagation of the ICON-
 373 QBO in the lowermost stratosphere. Instead, the downward propagation of the ICON-
 374 QBO stops well above the tropopause, while the ERA5-QBO propagates down to the
 375 tropopause.

376 4 The momentum budget of the ICON-QBO in the TEM framework

377 To understand why the ICON-QBO shows the pronounced lack of downward propa-
 378 gation as identified in Section 3, we evaluate its zonal momentum budget in the TEM
 379 framework calculated as described in Section 2.3.2.

380 4.1 Spatio-temporal structure of the TEM forcing in the equatorial strato- 381 sphere in the ICON simulation

382 Figure 3 shows the time-altitude cross sections of the stratospheric 5° S– 5° N mean
 383 zonal wind tendencies in the TEM framework. In general, the spatio-temporal structure
 384 of the various TEM tendencies corresponds well to the standard QBO paradigm. The

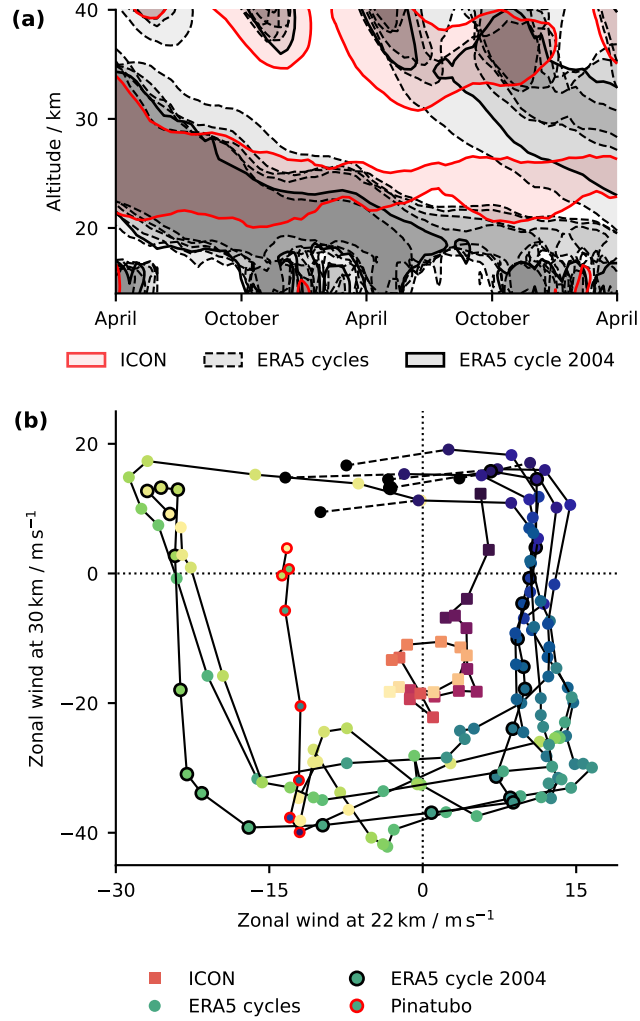


Figure 2. (a) Time-altitude cross section of the 5°S – 5°N daily mean zonal wind of the ICON simulation and the six individual QBO cycles of the ERA5-QBO-ensemble, starting on April 1 of the years 1985, 1990, 1997, 2004, 2008, and 2013. The shading highlights westerlies, and the contour lines mark the 0 m s^{-1} -isotach, with the ERA5 QBO cycle starting on April 1, 2004 being highlighted by a solid black contour. (b) Temporal trajectory of pairs of 5°S – 5°N monthly mean zonal wind at $\sim 22\text{ km}$ and $\sim 30\text{ km}$ for the ICON simulation and the six individual QBO cycles of the ERA5-QBO-ensemble, starting in April of the years 1985, 1990, 1997, 2004, 2008, and 2013. The trajectories start at the dark points, and for the ERA5-QBO-ensemble, the very first dark point, which is connected by a dashed line, marks the wind pair of March prior the "official" two-year-period starts. In the ERA5 QBO cycle starting on April 1, 1990, months after the eruption of Mt. Pinatubo in June 1991 are highlighted by red circles.

385 zonal wind tendency due to the vertical EP flux divergence is centered in the shear zones
 386 of the ICON-QBO and acts to drive their downward propagation (Fig. 3c). In contrast,
 387 the zonal wind tendency due to vertical residual advection acts against the downward
 388 propagation of the QBO shear zones, especially that of the easterly shear zone, which
 389 is initially located between 30 km and 38 km (Fig. 3a). The zonal wind tendency due to
 390 meridional advection is negligibly small in the shear zones of the ICON-QBO and is only
 391 relevant for the dynamics of the SAO (Fig. 3b). The zonal wind tendency due to the merid-

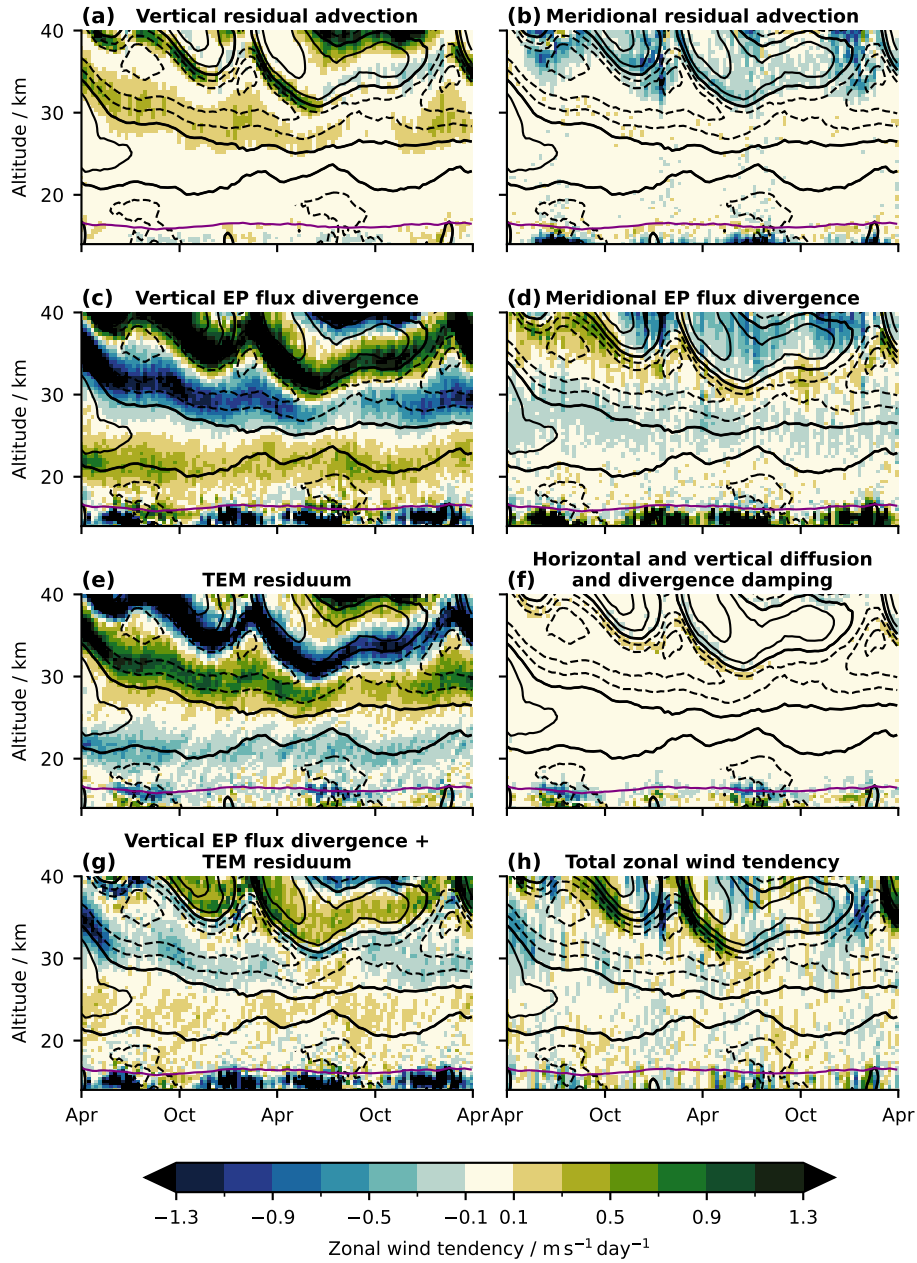


Figure 3. Time-altitude cross section of the 5°S – 5°N mean weekly-averaged TEM zonal wind tendencies in the ICON simulation starting on April 01, 2004: (a,b) zonal wind tendency due to vertical and meridional residual advection, respectively, (c,d) zonal wind tendency due to vertical and meridional EP flux divergence, respectively, (e) TEM residuum, (f) zonal wind tendency due to horizontal and vertical diffusion and divergence damping, (g) sum of the zonal wind tendency due to vertical EP flux divergence and the TEM residuum, and (h) the total zonal wind tendency. Black contour lines show isotachs of the 5°S – 5°N mean zonal wind in intervals of 10 m s^{-1} with negative values being dashed, positive values being solid, and the 0 m s^{-1} -isotach being bold solid. Purple contours mark the 370 K-isentrope, which is a proxy for the tropopause altitude.

392 zonal EP flux divergence is strongest in the shear zones above ~ 25 km (Fig. 3d), where
 393 it facilitates the downward propagation of the zonal wind jets, in particular those of the
 394 SAO. Below 25 km, the zonal wind tendency due to meridional EP flux divergence is small
 395 overall. All of these findings highlight that the basic dynamics of the QBO are well cap-
 396 tured by the global storm-resolving ICON simulation.

397 However, the sum of all TEM tendencies does not match the total zonal wind ten-
 398 dency of the ICON simulation (Fig. 3h). Consequently, the TEM zonal momentum bud-
 399 get of the ICON-QBO is closed by a large residuum (Fig. 3e). Figure 3 shows that the
 400 residuum strongly counteracts the zonal wind tendency due to vertical EP flux diver-
 401 gence. This strong cancellation between the vertical EP flux divergence and the residuum
 402 is very similar to the findings of Yao and Jablonowski (2013, 2015). They argue that the
 403 strong residuum of the TEM momentum budget is due to the direct effect of implicit and
 404 explicit diffusion on the QBO jets. This attribution is questionable for the ICON sim-
 405 ulation, since the zonal wind tendency due to explicit diffusive processes (i.e., horizon-
 406 tal diffusion, divergence damping, parameterized vertical diffusion) in the equatorial strato-
 407 sphere is negligibly small throughout the entire simulation, except for the tropopause
 408 region and the shear zones below the SAO jets, and clearly cannot explain the TEM residuum
 409 (Fig. 3f). Apparently, explicit diffusive processes do not directly damp the jets of the
 410 ICON-QBO. Therefore, we conclude that too strong explicit diffusive processes are not
 411 the root cause of the lack of downward propagation of the ICON-QBO in the sense that
 412 they directly damp the QBO.

413 Based on the results of Yao and Jablonowski (2013, 2015), the negligible contri-
 414 bution of explicit diffusive processes to the TEM residuum would suggest that the TEM
 415 residuum is mainly the imprint of implicit diffusion of ICON’s dynamical core. Never-
 416 theless, we further speculate that the TEM residuum in the ICON simulation may have
 417 non-physical causes. Detailed analysis has provided some evidence that the ICON sim-
 418 ulation suffers from numerical noise, which appears as spurious features in the simulated
 419 atmospheric flow, including the horizontal and vertical wind components. Therefore, the
 420 noise is sampled by the instantaneous TEM diagnostics, which diagnose the spurious flow
 421 features as a physical signal. This could ultimately lead to an overestimation of the ver-
 422 tical component of the EP flux and its divergence. However, if the noise is generated in-
 423 situ at individual model levels and does not propagate upward, the divergence of the over-
 424 estimated vertical EP flux would be purely diagnostic and would not correspond to wave-
 425 mean flow interactions of a vertically propagating wave, which accelerates the mean flow.
 426 In that case, the TEM momentum budget must be closed by a huge residuum. Addition-
 427 ally, the TEM residuum may be in part an artefact of the remapping of the model out-
 428 put from ICON’s native grid to the n256 Gaussian analysis grid. Ultimately, the exact
 429 root cause of the TEM residuum in the ICON simulation is still unclear and its more de-
 430 tailed analysis is a clear target for future research.

431 Given the strong cancellation between the zonal wind tendency due to vertical EP
 432 flux divergence — that is, the vertical wave forcing of the ICON-QBO — and the TEM
 433 residuum, we compute their sum to obtain an *effective vertical wave forcing* (Fig. 3f).
 434 The magnitude of the effective vertical wave forcing looks much more reasonable com-
 435 pared to the remaining TEM zonal wind tendencies than the actual vertical wave forc-
 436 ing. The effective vertical wave forcing also acts to drive a downward propagation of the
 437 shear zones of the ICON-QBO, indicating that the actual vertical wave forcing slightly
 438 overcompensates for the residuum.

439 4.2 Comparison with the TEM momentum budget of the ERA5-QBO

440 According to the standard QBO paradigm, a lack of downward propagation of the
 441 QBO jets can have two possible root causes: a too strong tropical upwelling as part of
 442 a too strong Brewer-Dobson circulation (BDC), or a too weak vertical wave forcing, i.e.

443 in our case too weak effective vertical wave forcing. In the following, we will investigate
 444 which of these two root causes is responsible for the lack of downward propagation of
 445 the ICON-QBO by comparing its TEM momentum budget with that of the ERA5-QBO.

446 For the comparison of QBO momentum budgets, it is essential that they are calculated
 447 for the same phase of the QBO. This is usually achieved by constructing so-called
 448 QBO composites, which are averages over several QBO cycles referenced at a fixed altitude
 449 based on a certain criterion (see, e.g., Krismer & Giorgetta, 2014; Bushell et al.,
 450 2020). However, due to the comparatively short simulation period of the ICON simulation,
 451 this methodology is not applicable for us. Instead, we compare the momentum
 452 budgets of the ICON-QBO and the ERA5-QBO for a fixed period, which is already well
 453 away from the initialization of the ICON simulation, but during which both QBOs are

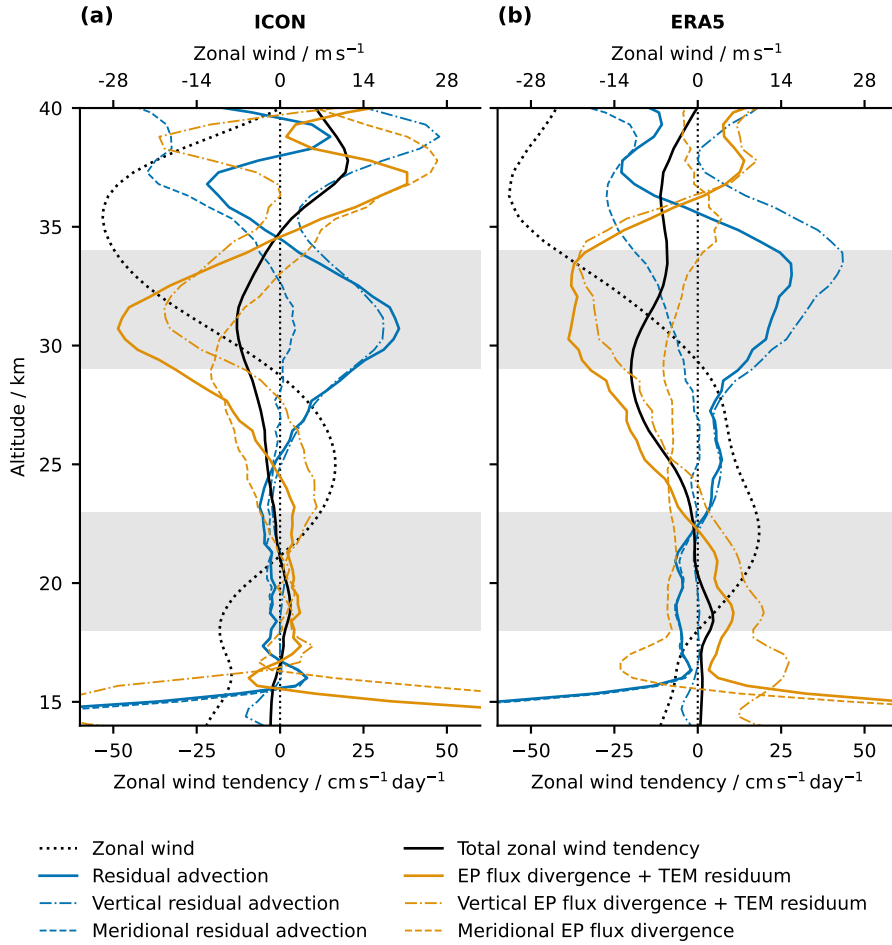


Figure 4. 5°S – 5°N mean profiles of the TEM zonal wind tendencies averaged over the period May 17, 2004–October 07, 2004 in (a) the ICON simulation and in (b) the ERA5 reanalysis. Please note that the *residual advection* (solid blue curve) is the sum of the *vertical residual advection* (dashed-dotted blue curve) and the *meridional advection* (dashed blue curve), and that the *EP flux divergence + TEM residuum* (solid orange curve) is the sum of the *vertical EP flux divergence + TEM residuum* (dashed-dotted orange curve) and the *meridional EP flux divergence* (dashed orange curve). The x-axis for the zonal wind \bar{u} is given at the upper spine. Light gray bars mark the altitude ranges of the lower and upper shear zones in Figure 5.

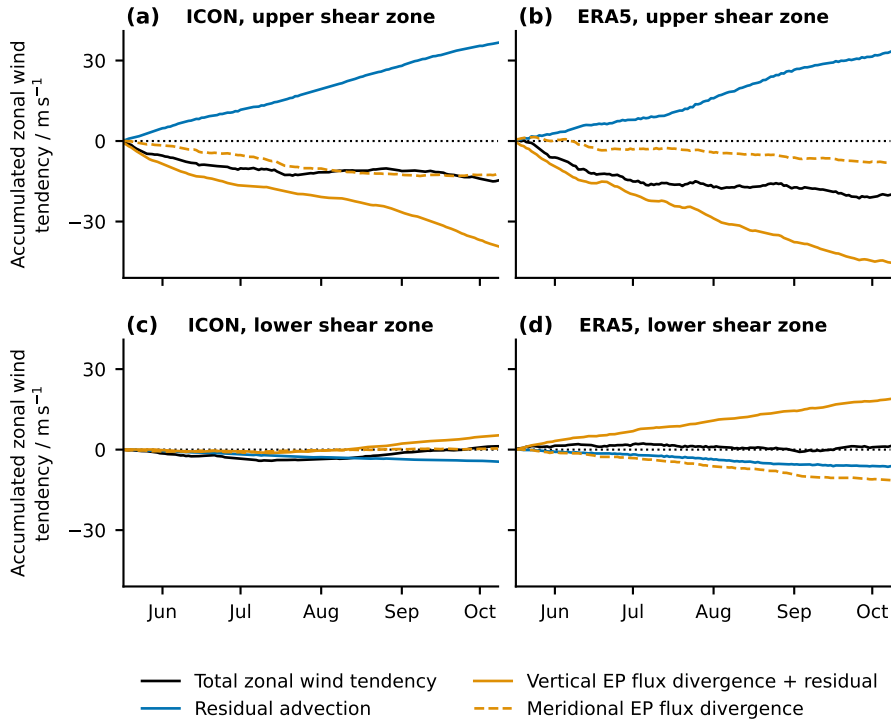


Figure 5. Accumulated 5°S – 5°N mean TEM zonal wind tendencies during May 17, 2004–October 07, 2004 for (a,c) the ICON simulation and (b,d) the ERA5 reanalysis. Panels (a,b) show tendencies averaged between an altitude of 29 km and 34 km, which is representative of the upper QBO shear zone during the accumulation period, and panels (c,d) show tendencies averaged between an altitude of 18 km and 23 km, which is representative of the lower QBO shear zone during the accumulation period. These altitude ranges are highlighted in Figure 4.

454 still reasonably close to each other. For this purpose, we choose the period May 17, 2004–
 455 October 07, 2004, which is highlighted by the vertical dashed lines in Figure 1. By do-
 456 ing the comparison for a fixed period, we also ensure that both, the ICON-QBO and the
 457 ERA5-QBO have the same seasonal boundary conditions.

458 Figure 4 shows the TEM momentum budgets of the ICON-QBO and the ERA5-
 459 QBO averaged over the analysis period May 17, 2004–October 07, 2004 as a function of
 460 altitude. Figure 5 shows the accumulated TEM tendencies in the upper (29 km–34 km)
 461 and lower (18 km–23 km) shear zones of the ICON-QBO and the ERA5-QBO. Both fig-
 462 ures indicate that a too strong tropical upwelling is not the root cause for the lack of down-
 463 ward propagation of the ICON-QBO. Throughout the whole QBO domain (17 km–35 km),
 464 the zonal wind tendency due to residual advection, which is dominated by its vertical
 465 component, is of comparable magnitude for the ICON-QBO and the ERA5-QBO (Fig. 4).
 466 Also in both shear zones, the accumulated tendency due to residual advection is in good
 467 agreement between the ICON simulation and the ERA5 reanalysis (Fig. 5).

468 This finding is confirmed by Figure 6, which shows the residual vertical velocity
 469 w^* averaged over the simulation period. The 30°S – 30°N mean w^* , a proxy for the strength
 470 of the rising branch of the BDC, is weaker in the ICON simulation than in the ERA5
 471 reanalysis at all altitudes, except for two narrow regions around 25 km and 34 km. The
 472 5°S – 5°N mean w^* , which is ultimately relevant for the QBO, is also weaker in ICON
 473 than in ERA5 at all altitudes, except for the altitudes between 24 km and 28.5 km. The

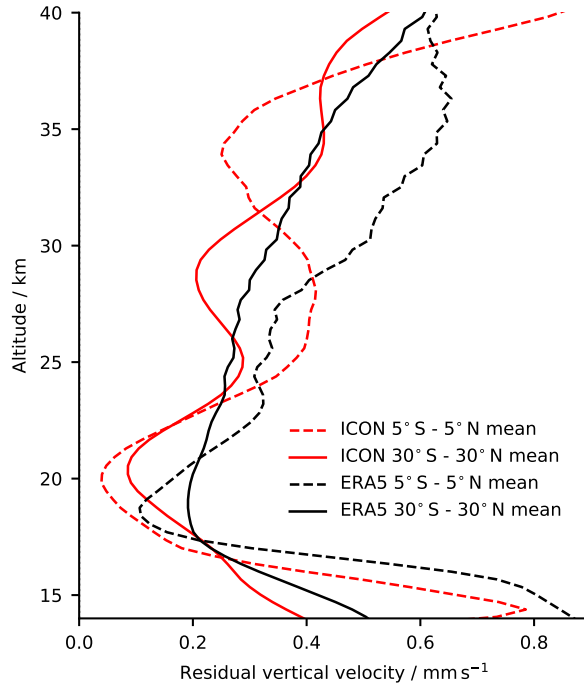


Figure 6. Residual vertical velocity w^* of the ICON simulation and the ERA5 reanalysis averaged over the period April 01, 2004–March 31, 2006.

474 oscillating vertical structure of the w^* profiles in the ICON simulation, which causes them
 475 to locally exceed those of the ERA5 reanalysis, is the imprint of the persistent secondary
 476 meridional circulation (SMC) of the stalling ICON-QBO itself. We conclude that the trop-
 477 ical upwelling associated with the BDC is not too strong in the ICON simulation, but
 478 rather too weak compared to the ERA5 reanalysis. Therefore, it cannot be the root cause
 479 of the lack of downward propagation of the ICON-QBO.

480 Before we proceed with the comparison of the wave forcing between the ICON-QBO
 481 and the ERA5-QBO, it should be mentioned that it is reasonable to consider the sum
 482 of the zonal wind tendency due to the vertical EP flux divergence and the TEM residuum
 483 as the effective vertical wave forcing also in the ERA5 reanalysis. In ERA5, the TEM
 484 residuum is dominated by the zonal wind tendency of the GW parameterization, so the
 485 effective vertical wave forcing represents the total zonal forcing due to vertically prop-
 486 agating waves. So even though the details of the effective vertical wave forcing differ be-
 487 tween ICON and ERA5, it is a reasonable measure of the total vertical wave forcing in
 488 both cases. Therefore, it is meaningful to compare the effective vertical wave forcing be-
 489 tween ICON and ERA5.

490 In the upper shear zone, the effective vertical wave forcing is in good agreement
 491 between the ICON simulation and the ERA5 reanalysis (Fig. 5a,b). This corresponds
 492 well to the overall reasonable downward propagation of this shear zone in the first year
 493 of the ICON simulation (Fig. 1). In contrast, the effective vertical wave forcing in the
 494 lower shear zone is much weaker in the ICON simulation than in the ERA5 reanalysis,
 495 and at the end of the analysis period the accumulated effective vertical wave forcing is
 496 more than three times weaker in ICON than in ERA5 (Fig. 5c,d). This shows that the
 497 root cause of the lack of downward propagation of the ICON-QBO in the lowermost strato-
 498 sphere is a too weak effective vertical wave forcing.

499 The zonal wind tendency due to meridional EP flux divergence differs qualitatively
 500 between the ICON simulation and the ERA5 reanalysis. In ERA5, it is approximately
 501 constant throughout the whole QBO domain between 18 km and 34 km (Fig. 4b), while
 502 in ICON it clearly depends on altitude and shows a local maximum in the upper shear
 503 zone at ~ 30 km (Fig. 4a). As a consequence, the accumulated zonal wind tendency due
 504 to meridional EP flux divergence in the upper shear zone is twice as large in ICON as
 505 in ERA5 at the end of the analysis period (Fig. 5a,b). This shows that the meridional
 506 wave forcing is obviously important for the ICON-QBO and contributes significantly to
 507 the downward propagation of the upper shear zone.

508 Overall, we conclude that the TEM momentum balance of the ICON-QBO in the
 509 upper QBO domain during the analysis period is reasonable. Here, the residual advec-
 510 tion, the effective vertical wave forcing, and the total zonal wind tendency show good
 511 quantitative agreement with ERA5 (Fig. 5a,b). In contrast, the wave forcing of the ICON-
 512 QBO in the lowermost stratosphere is essentially zero and thus substantially weaker than
 513 in ERA5, leading to a biased QBO momentum balance. The root cause of the lack of
 514 downwelling of the ICON-QBO is a lack of effective vertical wave forcing in the lower-
 515 most stratosphere.

516 4.3 Spectral decomposition of the QBO wave forcing

517 So far, we have only considered the total wave forcing, which does not allow any
 518 conclusions to be drawn about the types and scales of the waves driving the ICON-QBO.
 519 To understand which part of the wave spectrum is responsible for the lack of vertical wave
 520 forcing in the ICON simulation, we compute zonal wavenumber-frequency spectra of the
 521 vertical EP flux and its divergence for 20 non-overlapping, non-tapered 36-day windows
 522 spanning the period April 11, 2004–March 31, 2006 (see Sec. 2.3.2 for details). Subse-
 523 quently, we sum the spectra over certain zonal wavenumber and ground-based zonal phase
 524 speed ranges corresponding to different wave types (see Tab. 1). The time-altitude cross
 525 section of the vertical EP flux divergence in the tropical stratosphere associated with these
 526 wave types in the ICON simulation and in the ERA5 reanalysis is shown in Figure 7 for
 527 eastward propagating waves and in Figure 8 for westward propagating waves. Note that
 528 we omit waves with $|k| > 100$ from the analysis because the zonal wavenumber-frequency
 529 spectrum of the vertical EP flux in the ICON simulation suffers from pronounced alias-
 530 ing at these scales (see Supporting Information). In addition, GCMs tend to underes-
 531 timate the vertical EP flux at zonal wavenumbers already well below the Nyquist wavenum-
 532 ber (Krismer et al., 2015), calling into question the reliability of the resolved wave mo-
 533 mentum flux in ERA5 for waves with $|k| > 100$.

Table 1. Zonal wavenumber and ground-based zonal phase speed ranges corresponding to different wave types for which we compute the vertical EP flux and its divergence. Please note that the sampling interval of the data of 3 h does only allow for the detection of waves with a frequency of < 4 cpd. Thus, the largest detectable ground-based zonal phase speed of waves with $|k| = 100$ is 18.5 m s^{-1} .

Wave type	Zonal wavenumber (eastward)	Zonal wavenumber (westward)	Ground-based zonal phase speed
Slow planetary-scale	$1 \leq k \leq 18$	$-18 \leq k \leq -1$	$ c \leq 20 \text{ m s}^{-1}$
Fast planetary-scale	$1 \leq k \leq 18$	$-18 \leq k \leq -1$	$ c > 20 \text{ m s}^{-1}$
Intermediate-scale	$19 \leq k \leq 100$	$-100 \leq k \leq -19$	–

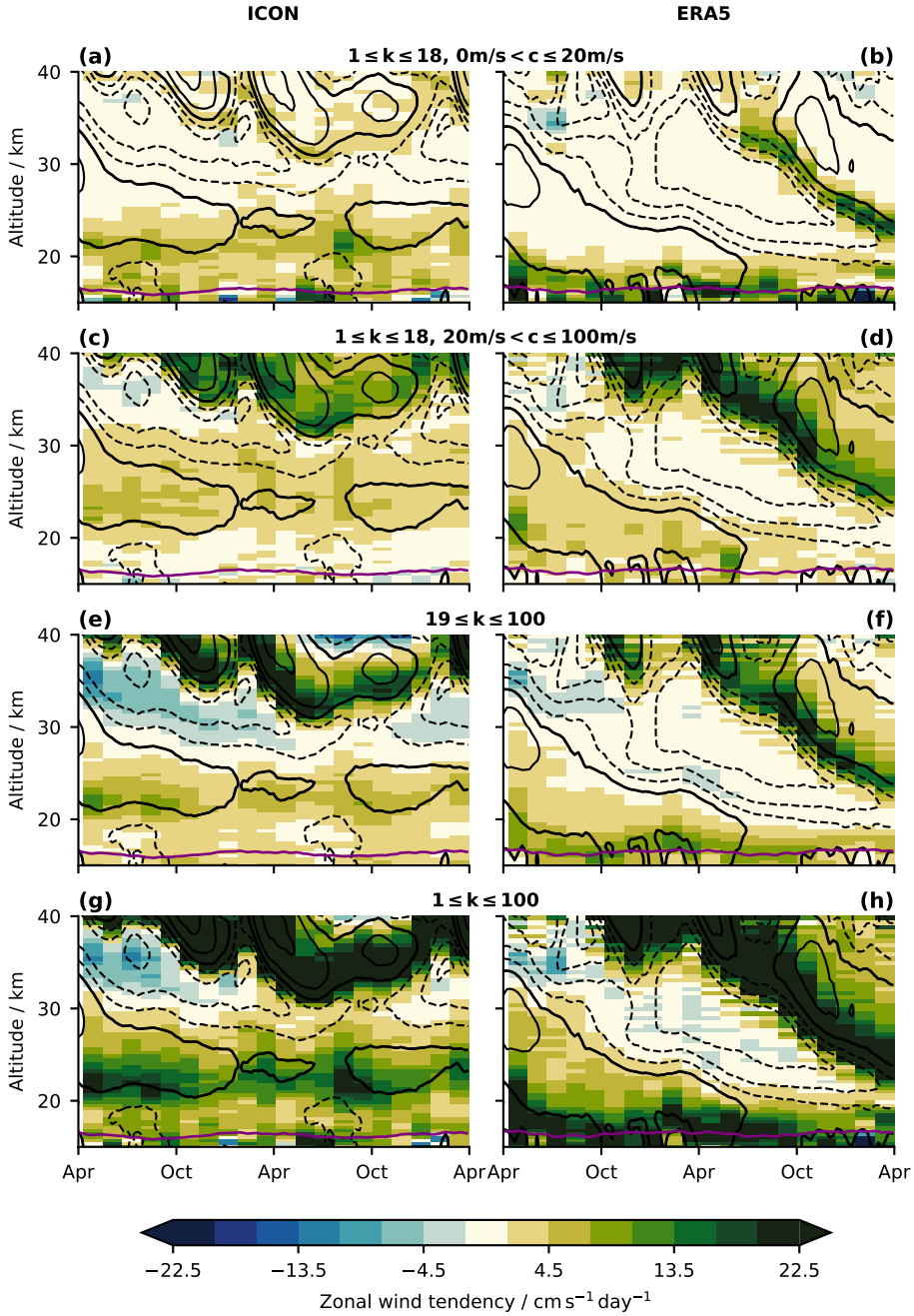


Figure 7. Time-altitude cross sections of the 10° S– 10° N mean zonal wind tendency due to vertical EP flux divergence associated with eastward propagating waves for (left panels) the ICON simulation and (right panels) the ERA5 reanalysis, separated into different wave types as defined in Tab. 1: (a,b) slow planetary-scale waves, (c,d) fast planetary-scale waves, (e,f) intermediate-scale waves, (g,h) sum of slow planetary-scale, fast planetary-scale, and intermediate-scale waves. The purple contour lines mark the 370 K-isentrope, which is a proxy for the tropopause altitude.

534
535

Figure 7 shows that the absolute magnitude of the zonal wind tendency due to vertical EP flux divergence associated with slow eastward propagating planetary-scale waves,

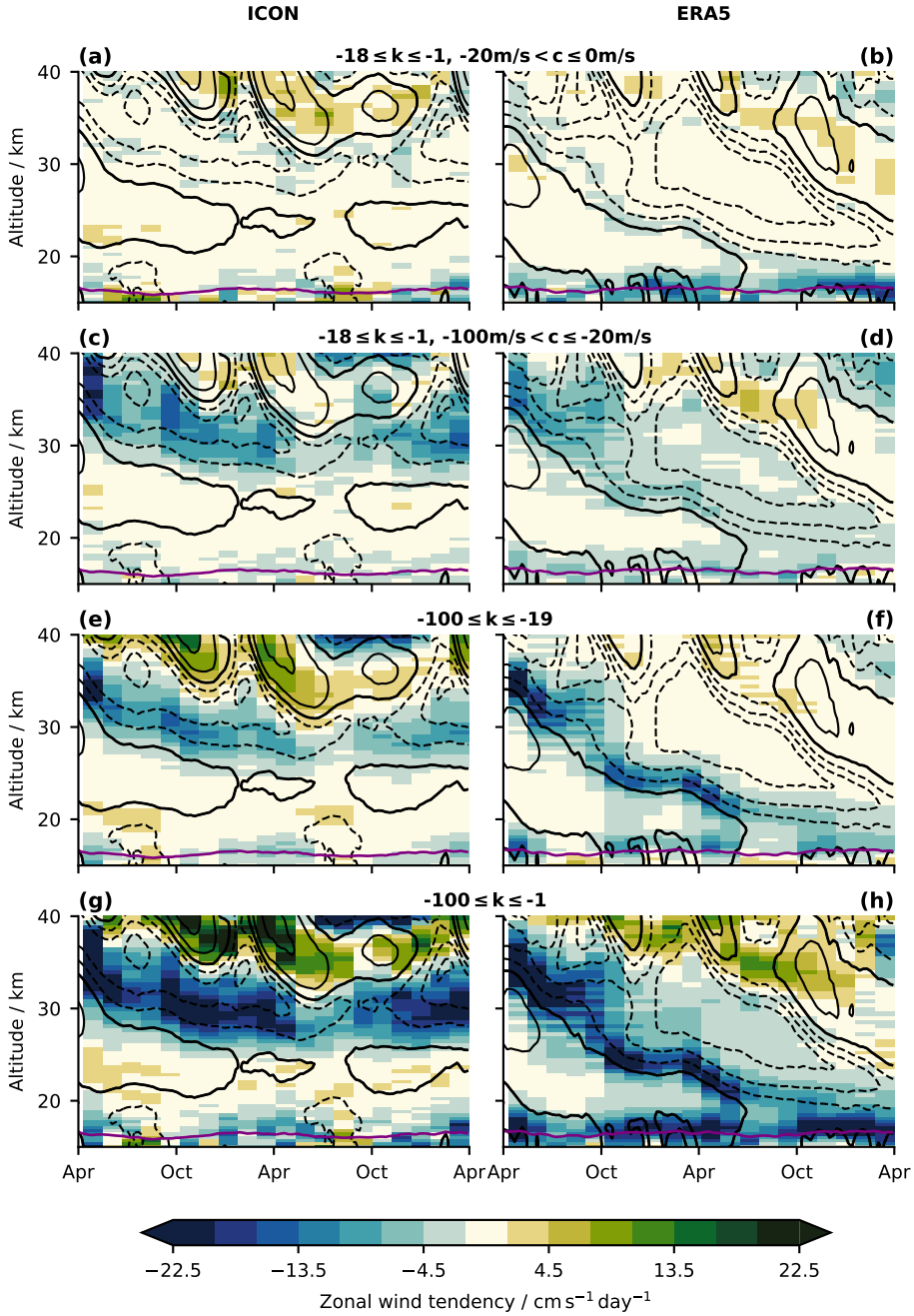


Figure 8. As Figure 7, but for westward propagating waves.

536 i.e. slow equatorial Kelvin waves, in the lower westerly shear zone (i.e. 18 km–23 km) is
 537 much weaker in the ICON simulation than in the ERA5 reanalysis. In the ICON sim-
 538 ulation, the wave forcing is further distributed rather uniformly over a wide vertical range
 539 (~17 km–25 km), while in the ERA5 reanalysis it is strongly concentrated in the westerly
 540 shear zone in the lowermost stratosphere. These findings suggest that the lack of
 541 vertical wave forcing of the ICON-QBO is predominantly due to slow eastward propa-
 542 gating planetary-scale waves. However, the large vertical spread of the vertical wave forc-
 543 ing by those waves in the ICON simulation — and thus the overall weaker eastward wave

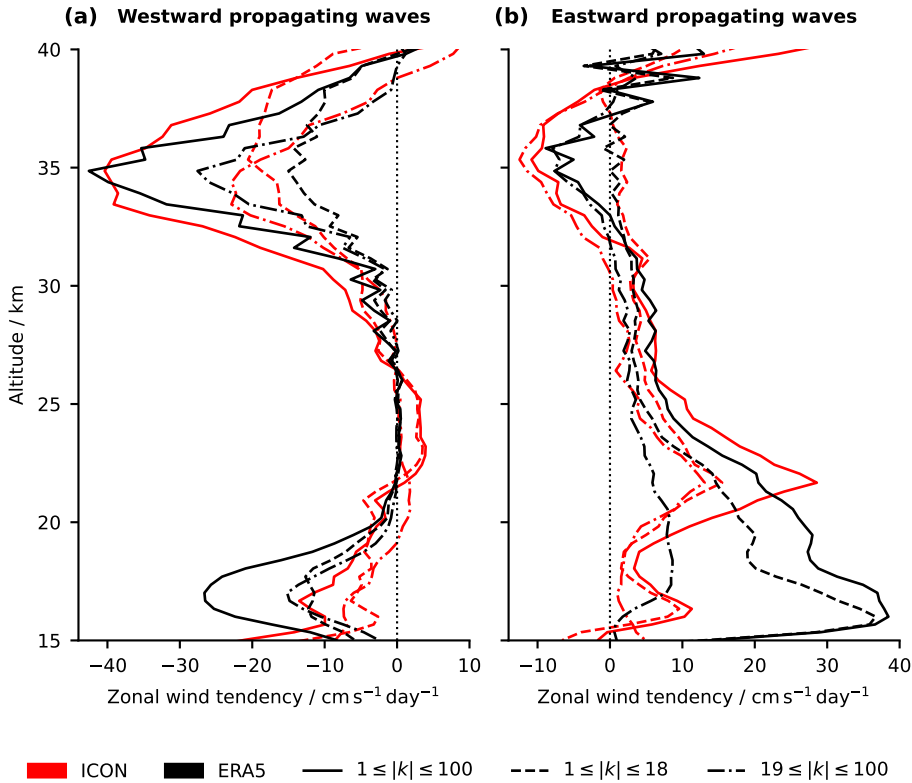


Figure 9. Profiles of the 10°S – 10°N mean zonal wind tendency due to the vertical EP flux divergence associated with (a) westward propagating waves and (b) eastward propagating waves of different zonal wavenumber ranges in the period April 11, 2004–May 16, 2004. The vertical black dotted line marks a zonal wind tendency of $0\text{ m s}^{-1}\text{ day}^{-1}$.

544 forcing in the lower westerly shear zone (i.e. 18 km–23 km) compared to ERA5 (Fig. 7g,h)
 545 — can also be partly attributed to the weak westerly jet of the ICON-QBO itself. The
 546 weak westerly jet only allows very slow waves with a ground-based zonal phase speed
 547 close to 0 m s^{-1} to dissipate in the shear zone below it, while faster waves can propagate
 548 through. Consequently, it is not immediately clear from Figure 7 whether the weak east-
 549 ward wave forcing in the lower westerly shear zone (i.e. 18 km–23 km) is the cause or the
 550 effect of the weak westerly jet and its lack of downward propagation.

551 Therefore, we analyze the vertical wave forcing during the first of the 20 windows
 552 used for spectral analysis, i.e. April 11, 2004–May 16, 2004 (Fig. 9). During this period,
 553 the vertical structure of the ICON-QBO and the magnitude of its jets still agree reason-
 554 ably well with those of the ERA5-QBO (Fig. 1), allowing for a much clearer attribution
 555 of cause and effect. As shown in Figure 9b, the total vertical wave forcing by eastward
 556 propagating waves with $|k| < 100$ in the lowermost stratosphere is substantially weaker
 557 in the ICON simulation than in ERA5, and the majority of this difference is attributable
 558 to planetary-scale waves. Therefore, we conclude that lack of downward propagation of
 559 the ICON-QBO is mainly due to a lack of vertical wave forcing by slow eastward prop-
 560 agating planetary-scale waves, i.e. slow equatorial Kelvin waves.

561 The vertical wave forcing by eastward propagating intermediate-scale waves behaves
 562 very similar to that by slow eastward propagating planetary-scale waves (Fig. 7e,f). Again,
 563 the absolute magnitude of the wave forcing in the lower westerly shear zone (i.e. 18 km–

23 km) is weaker in the ICON simulation than in the ERA5 reanalysis, and it is distributed over a larger vertical range. Obviously, the lack of downward propagation of the ICON-QBO in the lowermost stratosphere is in part also attributable to this wave type. In contrast, the magnitude of the vertical wave forcing of the ICON-QBO by fast eastward propagating planetary-scale waves, i.e. fast equatorial Kelvin waves, is overall comparable to that of the ERA5-QBO (Fig. 7c,d). However, in the ICON simulation a large fraction of this wave forcing also occurs in the easterly shear zone between ~ 25 km and ~ 31 km, and thus opposes the downward propagation of this shear zone. We think that this is likely one reason for the lack of downward propagation of the upper easterly jet of the ICON-QBO in the second year of the simulation.

For westward propagating waves (Fig. 8), the differences between the ICON simulation and the ERA5 reanalysis are smaller than for eastward propagating waves. For both the ICON-QBO and the ERA5-QBO, slow westward propagating planetary-scale waves, including $n=0$ equatorial Rossby waves, do not contribute to the downward propagation of the easterly shear zone, which is initially located between 30 km and 38 km (Fig. 8a,b). In contrast, the downward propagation of this shear zone is mainly driven by fast westward propagating planetary-scale waves, including mixed Rossby-gravity waves (Fig. 8c,d), and by intermediate-scale westward-propagating waves (Fig. 8e,f) for both the ICON-QBO and the ERA5-QBO. The vertical wave forcing by these two wave types is in good agreement between the ICON simulation and the ERA5 reanalysis, given the different spatio-temporal structure of their QBOs. This is confirmed by Figure 9a, which also shows reasonable agreement between the vertical wave forcing by westward propagating waves in the ICON simulation and ERA5 during the first of the 20 windows used for spectral analysis, i.e. April 11, 2004–May 16, 2004.

5 Evaluation of the tropical wave field in the ICON simulation

In the previous section, we showed that the lack of downward propagation of the ICON-QBO in the lowermost stratosphere is due preferably to a lack of vertical wave forcing, i.e. a lack of vertical EP flux divergence, associated with eastward propagating planetary-scale waves, mainly comprising equatorial Kelvin waves. In principle, a lack of vertical wave forcing of the QBO can have three possible root causes: (1) a misrepresentation or lack of wave generation in the troposphere, (2) a misrepresentation or lack of vertical wave propagation from the troposphere into the stratosphere, and (3) a misrepresentation or lack of wave dissipation and damping in the shear zones of the QBO. Here, we investigate which of these possible root causes is responsible for the lack of vertical wave forcing in the ICON simulation.

5.1 Dissipation and damping of SEWs in the lowermost stratosphere

To analyze the damping and dissipation of SEWs in the ICON simulation, we follow the methodology of Krismer and Giorgetta (2014, see their Sec. 5 c), and consider four different processes: the damping and diffusion of wave-induced zonal wind perturbations by (1) divergence damping, (2) explicit horizontal diffusion, and (3) parameterized vertical diffusion, as well as (4) the damping of wave-induced temperature perturbations by longwave radiation. First, we compute the amplitude spectra of the tendency variables associated with these four processes and the corresponding state variable on which the tendency variable acts, as a function of zonal wavenumber and frequency. The spectra are computed for four non-overlapping and non-tapered 36-day windows spanning the period May 17, 2004–October 07, 2004, which is the same period we used to compare the zonal momentum budgets of the ICON-QBO and the ERA5-QBO (see Sec. 4.2). We then average the spectra over all windows and over the 10° S– 10° N region. Since we are interested in the damping and dissipation of SEWs in the lower shear zone of the ICON-QBO, we further average the spectra over the 18 km–23 km altitude range (cmp. Sec. 4.2).

614 The spectra averaged in this way are shown in the left column panels of Figure 10. The
 615 right column panels of Figure 10 show the spectra of the quotient of the tendency vari-
 616 able and its corresponding state variable, which can be interpreted as the e -folding time
 617 of the particular dissipation or damping process associated with the tendency (see Kris-
 618 mer & Giorgetta, 2014). The shorter the e -folding time, the more efficient a particular
 619 dissipation or damping process is. In the following, we will analyze the dissipation and
 620 damping of large-scale waves, as they have been shown to be the root cause of the un-
 621 derestimation of the vertical wave forcing of the ICON-QBO.

622 The divergence damping appears to strongly damp very slow waves with $\omega < 0.5$ cpd
 623 and $|k| > 10$, while only leaving large-scale planetary waves with $|k| < 10$ and $\omega <$
 624 0.5 cpd nearly unaffected (Fig. 10b). This is due to the fact that the divergence damp-
 625 ing of the zonal wind depends strongly on frequency, but is more or less independent of
 626 zonal wavenumber (Fig. 10a). It is strongest for very slow or steady perturbations and
 627 decreases rapidly with increasing frequency. In principle, this behavior is to be expected
 628 because the divergence damping is employed in ICON to remove quasi-stationary small-
 629 scale checkerboard patterns. The spectrum of the parameterized vertical diffusion of the
 630 zonal wind also shows a first-order dependence on frequency, but it has a larger mag-
 631 nitude than the divergence damping, except for the lowest frequencies (Fig. 10c). As a
 632 result, parameterized vertical diffusion very efficiently damps all waves except large-scale
 633 planetary waves with $|k| < 10$ and $\omega < 0.5$ cpd (Fig. 10d). It further is the dominant
 634 damping mechanism for waves with $|k| > 15$ across the four mechanisms considered.
 635 The explicit horizontal diffusion of the zonal wind is virtually independent of frequency
 636 and zonal wavenumber and has a much smaller magnitude than the parameterized ver-
 637 tical diffusion and divergence damping over the entire spectral range considered (Fig. 10e).
 638 Therefore, explicit horizontal diffusion does not substantially damp waves with $|k| <$
 639 25 and $\omega < 1$ cpd (Fig. 10f). For waves with larger zonal wavenumbers and higher fre-
 640 quencies, wave damping by horizontal diffusion is still of secondary importance compared
 641 to wave damping by divergence damping and vertical diffusion. In contrast to the dif-
 642 fusive wave damping processes of the zonal wind, the radiative damping of waves depends
 643 mainly on intrinsic zonal phase speed and is most efficient for slow waves (Fig. 10h), which
 644 agrees with theory (e.g., Fels, 1982). Therefore, radiative damping is the dominant damp-
 645 ing mechanism of large-scale planetary waves with $|k| < 10$ and $\omega < 0.5$ cpd.

646 The basic result that planetary-scale waves with $|k| < 10$ and $\omega < 0.5$ cpd are
 647 mainly damped by radiation in the ICON simulation, while smaller-scale waves with $|k| >$
 648 10 and higher-frequency waves with $\omega > 0.5$ cpd are mainly damped by diffusive pro-
 649 cesses, agrees well with the results of Krismer and Giorgetta (2014). The overall damp-
 650 ing of large-scale waves in the lower shear zone of the ICON-QBO appears to be reason-
 651 able and not distorted. However, we found that the diffusive damping of waves in the
 652 ICON simulation is dominated by divergence damping and parameterized vertical dif-
 653 fusion instead of horizontal diffusion. It is unclear to what extent this partitioning of the
 654 diffusive wave damping in the ICON simulation is reasonable, and whether it indicates
 655 that individual diffusion and damping schemes are too strong or too weak. At least the
 656 divergence damping, which is implemented to reduce small-scale checkerboard patterns,
 657 has a surprisingly large impact on wave damping.

658 To validate these conclusions, we analyze the vertical propagation of exemplary Kelvin
 659 waves in physical space, which implicitly depends on all possible damping mechanisms
 660 present in ICON. Therefore, any gross misrepresentation of wave damping and dissipa-
 661 tion in ICON would become apparent in this representation. To isolate the Kelvin waves,
 662 we first computed the Fourier transform of the non-tapered but detrended symmetric
 663 perturbation temperature in longitude and time. The perturbation temperature is the
 664 deviation of the temperature from its zonal and temporal mean. Subsequently, we per-
 665 formed an inverse Fourier transform only on the spectral components with $1 \leq k \leq$

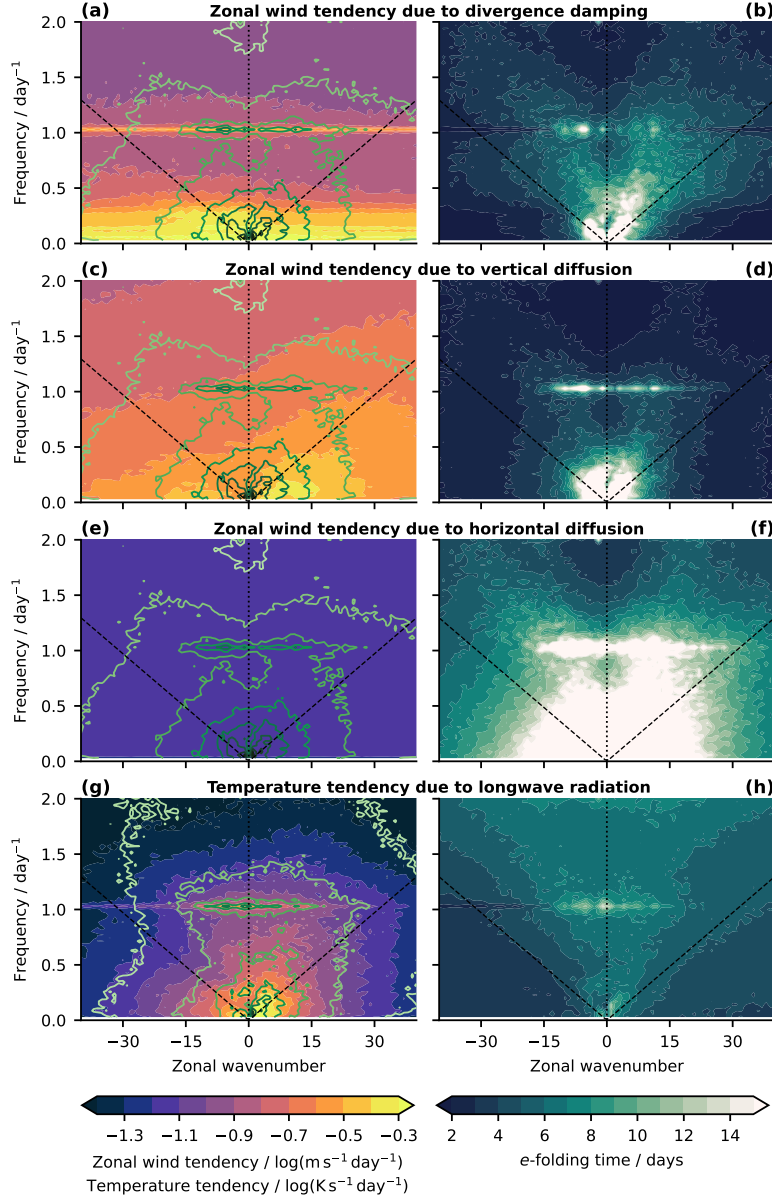


Figure 10. 10°S – 10°N mean zonal wavenumber–frequency spectra of (left panels) the amplitude of a particular tendency variable (colors) and its corresponding state variable (contours), and of (right panels) the quotient of this particular tendency variable and its corresponding state variable, i.e. the e -folding time. The spectra were computed for and averaged over four non-overlapping non-tapered 36-day windows during the period May 17, 2004–October 07, 2004. They were further averaged between 18 km and 23 km, which is representative of the lower shear zone of the ICON-QBO. Contour lines are logarithmic with an interval of (a,c,e) $0.3 \log(\text{m s}^{-1})$ and (g) $0.3 \log(\text{K})$ with darker lines indicating a larger amplitude. Panels (a,b) show the divergence damping of the zonal wind, (c,d) the explicit horizontal diffusion of the zonal wind, (e,f) the parameterized vertical diffusion of the zonal wind, and (g,h) the temperature tendency due to longwave radiation. Black dashed lines in all spectra mark lines of a constant zonal phase speed of $|c| = 15 \text{ m s}^{-1}$ for visual guidance.

666

$10, 0 \text{ cpd} < \omega \leq 0.4 \text{ cpd}$, and $0 \text{ m s}^{-1} < c \leq 10 \text{ m s}^{-1}$ (very slow Kelvin waves), $10 \text{ m s}^{-1} < c \leq 20 \text{ m s}^{-1}$ (slow Kelvin waves), and $20 \text{ m s}^{-1} < c \leq 50 \text{ m s}^{-1}$ (fast Kelvin waves).

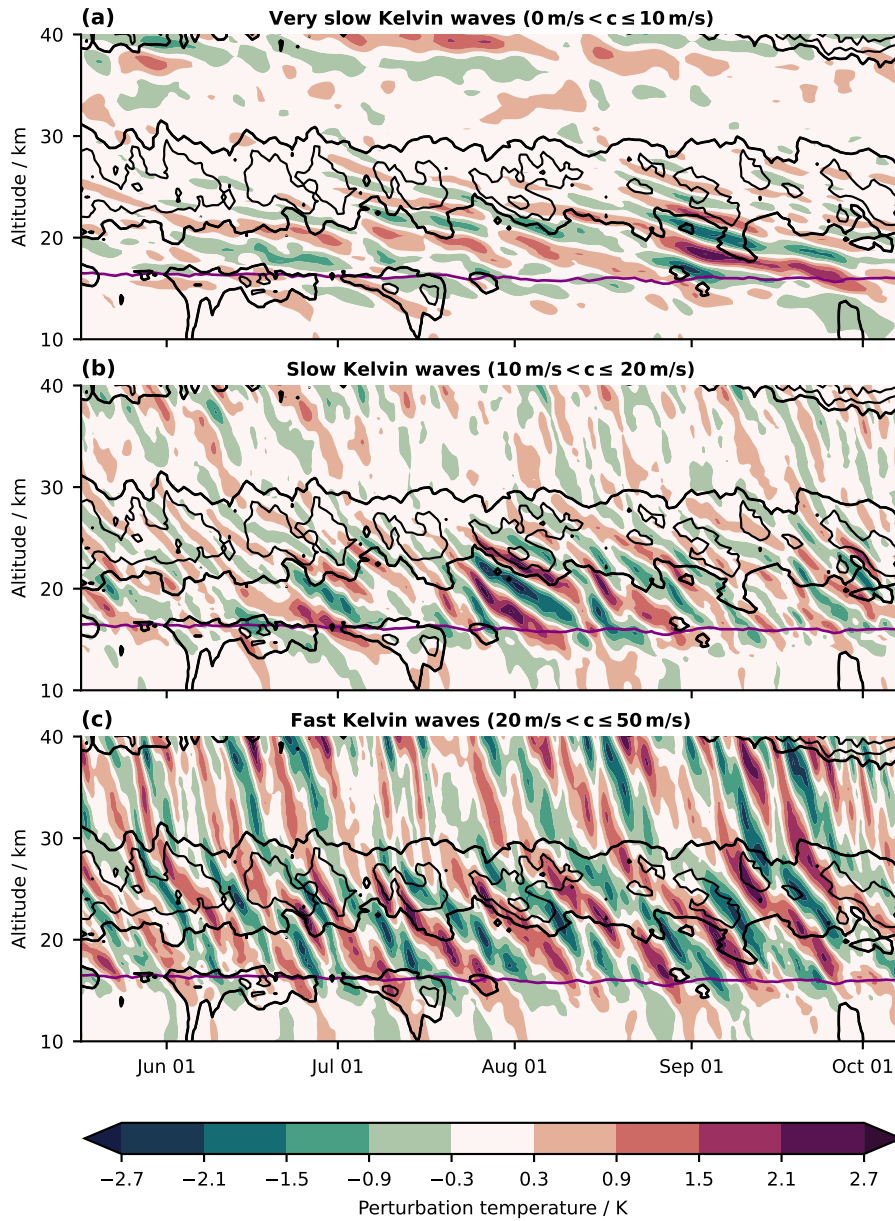


Figure 11. Time-altitude cross section of the temperature perturbations induced by (a) very slow Kelvin waves with $0 \text{ m s}^{-1} < c \leq 10 \text{ m s}^{-1}$, (b) slow Kelvin waves with $10 \text{ m s}^{-1} < c \leq 20 \text{ m s}^{-1}$, and (c) fast Kelvin waves with $20 \text{ m s}^{-1} < c \leq 50 \text{ m s}^{-1}$ in the ICON simulation during the period May 17, 2004–October 07, 2004 at 0.1756° N , 180° E . Black contour lines show daily mean westerly winds in intervals of 10 m s^{-1} , starting at 0 m s^{-1} (thick black contour). Contour lines for easterly winds are not plotted for clarity. The purple contour lines mark the 370 K -isentrope, which is a proxy for the tropopause altitude.

667

Figure 11 shows the vertical propagation of the equatorial Kelvin waves isolated in this way at a randomly selected equatorial location in the ICON simulation during May 17, 2004–October 07, 2004. The spatio-temporal structure of the three different classes of Kelvin waves is reasonable and agrees well with the standard theory of critical level filtering of vertically propagating waves. The filtering of Kelvin waves by the westerly jet of the ICON-QBO, which has a magnitude of 10 m s^{-1} – 20 m s^{-1} , clearly depends on their zonal phase speed. The very slow Kelvin waves are more or less completely damped in the lower part of the westerly jet and are absent above it. The slow Kelvin waves are also strongly damped in the westerly shear zone below the westerly jet, but there are still spurious small-amplitude signals of these waves above the westerly jet. The fast Kelvin waves, which do not reach their critical levels within the westerly jet, propagate through the jet without a substantial loss in amplitude. In general, except for the westerly shear zone between 18 km and 25 km, there is no substantial damping of the Kelvin waves. Therefore, we conclude that the vertical propagation of equatorial Kelvin waves in the stratosphere and their damping and diffusion are reasonably well represented in the ICON simulation. We rule out a gross misrepresentation of wave damping and propagation as the root cause of the lack of downward propagation of the ICON-QBO.

5.2 Vertical EP flux spectra in the lowermost stratosphere

In the following, we will analyze the vertical EP flux in the ICON simulation at an altitude of 17 km, just above the tropopause, because it allows us to analyze the upward propagating wave field before it interacts with the QBO jets. Thus, this analysis can reveal whether the lack of vertical wave forcing of the ICON-QBO is due to an underestimation of the wave momentum fluxes entering the stratosphere. As a first step, we compute the zonal wavenumber-frequency spectra of the vertical EP flux at 17 km for the same 20 non-overlapping, non-tapered 36-day windows spanning the period April 11, 2004–March 31, 2006 as in Section 4.3. We then average these spectra over all windows and over the 10° S – 10° N region.

Figure 12a,b shows the averaged spectra of the vertical EP flux of the ICON simulation and the ERA5 reanalysis. While the basic structure of both spectra agrees, there are notable differences between the ICON simulation and the ERA5 reanalysis. For the ERA5 reanalysis, the spectrum is much smoother than for the ICON simulation, and it shows some weak organization into a double-lobe structure along phase speeds close to $|c| = 30 \text{ m s}^{-1}$ and $|c| = 50 \text{ m s}^{-1}$. While the spectrum of the ICON simulation organizes along similar phase speed lines, it is substantially noisier than the spectrum of the ERA5 reanalysis. In addition, the spectrum of the ICON simulation is less powerful than that of the ERA5 reanalysis, especially at high frequencies of $\omega > 1 \text{ cpd}$. At these high frequencies, the vertical EP flux decreases rapidly in the ICON simulation and much faster than in the ERA5 reanalysis.

As shown in the Supporting Information, the noisy background in the ICON spectrum is the non-physical artefact of a too coarse temporal sampling interval, i.e. a too low output frequency. Our output frequency of 3 h is insufficient to sample fast and short GWs, which can have periods as short as 10 min. This leads to aliasing, which introduces substantial white noise to the spectrum of the vertical EP flux in the ICON simulation (cmp. Kirchner, 2005). The spectral noise inhibits a meaningful interpretation of the ICON spectrum for $|k| > 100$.

We further accumulate the averaged zonal wavenumber-frequency spectra of the vertical EP flux over all frequencies. The resulting zonal wavenumber spectra of the vertical EP flux of the ICON simulation and the ERA5 reanalysis are shown in Figure 12c. The spectra reveal that the vertical EP flux associated with small-scale GWs, i.e. waves with $|k| > 70$, is much larger for ICON than for ERA5 (Fig. 12c). This is explained by the much higher native resolution of the ICON simulation, which allows to resolve a sub-

719 stantially larger fraction of the GW spectrum than ERA5. As shown in Figure S3, it is
 720 explicitly not due to the previously discussed effect of temporal aliasing (cmp. Fig. S3).
 721 In contrast to small-scale GWs, for both westward and eastward propagating waves with
 722 $|k| < 70$, the vertical EP flux is substantially weaker in the ICON simulation than in
 723 the ERA5 reanalysis. For eastward propagating waves ($k > 0$), the vertical EP flux in
 724 the ICON simulation is about 20% weaker than in the ERA5 reanalysis, approximately
 725 uniformly over all zonal wavenumbers up to $k = 70$. For westward propagating waves
 726 ($k < 0$), the difference between the ICON simulation and the ERA5 reanalysis is even
 727 stronger, and the vertical EP flux in ICON is more than 40% weaker than in ERA5 for
 728 zonal wavenumbers between $k = -20$ and $k = -45$.

729 As the absolute magnitude of the vertical EP flux is generally much larger for planetary-
 730 scale waves ($|k| \lesssim 18$) than for smaller-scale waves (see Fig. 12c), the uniform relative
 731 underestimation of the vertical EP flux in the ICON simulation over a wide range of zonal
 732 wavenumbers means that — in absolute terms — the lack of incoming vertical EP flux
 733 is largest for planetary-scale waves, which is confirmed by Figure 12d. Therefore, the lack
 734 of — mainly planetary-scale — vertical wave forcing of the ICON-QBO (see Sec. 4.3)
 735 can ultimately be attributed to a lack of — mainly planetary-scale — vertical EP flux
 736 entering the lower stratosphere.

737 The fact that the underestimation of the vertical EP flux in the ICON simulation
 738 is even more pronounced for westward than for eastward propagating waves can be at-
 739 tributed to differences in upper-tropospheric wave filtering between ICON and ERA5.
 740 The ICON simulation has a substantial easterly bias in the upper troposphere and the
 741 tropopause region of up to -6 m s^{-1} compared to the ERA5 reanalysis (see Fig. 13). These
 742 easterlies in the ICON simulation result in a strong filtering of slow westward propagat-
 743 ing waves, which thus do not reach the lower stratosphere. The strong filtering of slow
 744 westward propagating waves in the ICON simulation can be seen in the zonal wavenumber-
 745 frequency spectrum of the vertical EP flux, which shows basically no westward, i.e. pos-
 746 itive, vertical EP flux for westward propagating waves with $-15 \text{ m s}^{-1} < c < 0 \text{ m s}^{-1}$
 747 (Fig. 12a, also cmp. Fig. 12b). This substantial lack of westward EP flux associated with
 748 slow westward propagating waves likely contributes to the lack of downward propaga-
 749 tion of the easterly shear zone of the ICON-QBO in the second year of the simulation
 750 (Fig. 1a). Here, the easterly jet becomes so weak that it can only effectively absorb west-
 751 ward propagating waves with $-15 \text{ m s}^{-1} < c < 0 \text{ m s}^{-1}$, which are mostly already fil-
 752 tered out in the upper troposphere. This leaves the easterly jet of the ICON-QBO with
 753 virtually no wave forcing.

754 5.3 Spectral variability of tropical precipitation and CCEWs

755 Most of the upward propagating tropical waves that drive the QBO are generated
 756 by latent heat release in deep tropical convection (Holton, 1972; Salby & Garcia, 1987;
 757 Ricciardulli & Garcia, 2000; Fritts & Alexander, 2003; Horinouchi et al., 2003). There-
 758 fore, the underestimation of the vertical EP flux entering the lowermost tropical strato-
 759 sphere, especially on planetary scales, indicates that wave generation in the tropical tro-
 760 posphere is likely underestimated in the ICON simulation. To investigate the wave sources
 761 in the ICON simulation in more detail, we will analyze the spectral variability of trop-
 762 ical precipitation, which is a widely used proxy for latent heating by tropical deep con-
 763 vection. Therefore, we computed zonal wavenumber-frequency spectra of precipitation
 764 for the ICON simulation, the ERA5 reanalysis, and the observational precipitation dataset
 765 IMERG, for 29 tapered 92-day windows with a 34-day overlap spanning the entire sim-
 766 ulation period from April 01, 2004–March 31, 2006. We then averaged these spectra over
 767 all 29 windows and between 15° S and 15° N , and the averaged spectra are shown in Fig-
 768 ure 14a-c.

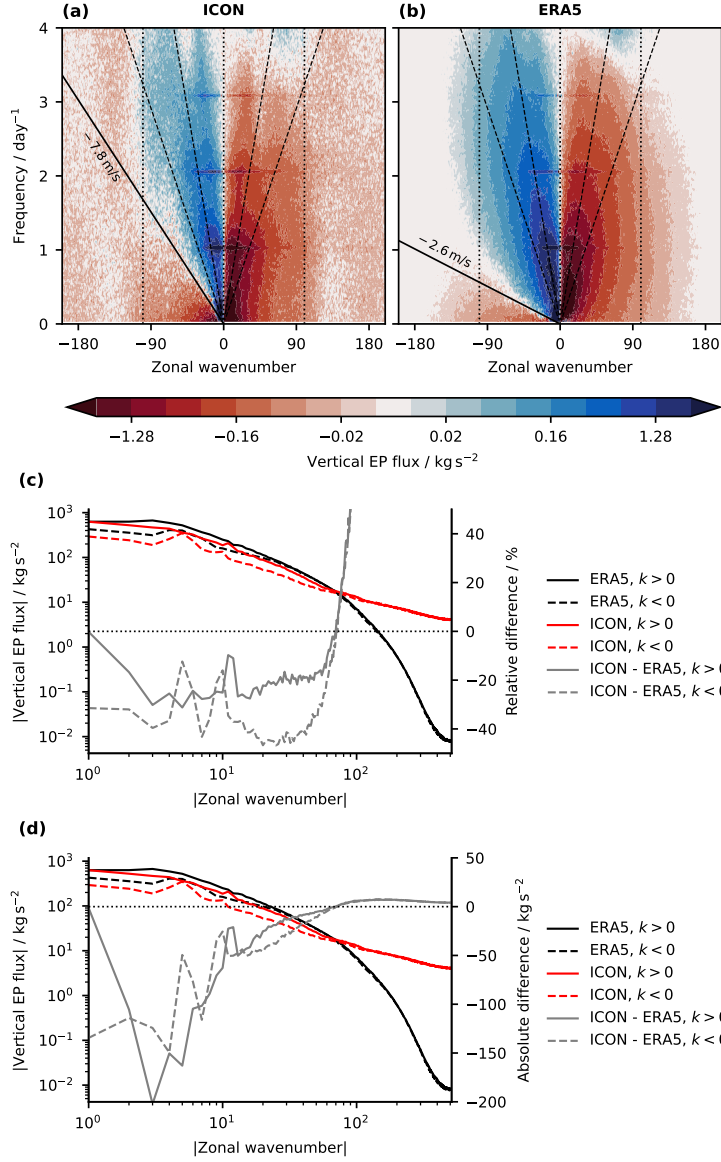


Figure 12. Spectral characterization of the 10° S– 10° N mean vertical EP flux at an altitude of 17 km, averaged over individual spectra calculated for 20 non-overlapping, non-tapered 36-day windows spanning the period April 11, 2004–March 31, 2006. Panels (a,b) show zonal wavenumber-frequency spectra for (a) the ICON simulation and (b) the ERA5 reanalysis. The solid black lines in panels (a,b) mark the zonal mean zonal wind at 17 km of the ICON simulation and the ERA5 reanalysis, respectively, while the dashed black lines mark lines of constant ground-based zonal phase speed of $|c| = 15 \text{ m s}^{-1}$ and $|c| = 30 \text{ m s}^{-1}$. The vertical dotted lines mark the zonal wavenumbers $|k| = 100$ and $k = 0$. Panels (c,d) show the zonal wavenumber spectra of the vertical EP flux in the ICON simulation and in ERA5, with panels (c) and (d) showing the relative and absolute difference between ICON and ERA5, respectively. In panels (c) and (d), the y-axis for the difference between ICON and ERA5 (gray curves) is given at the right spine, and the horizontal dotted line marks a relative and absolute difference of 0% and 0 kg s^{-2} , respectively.

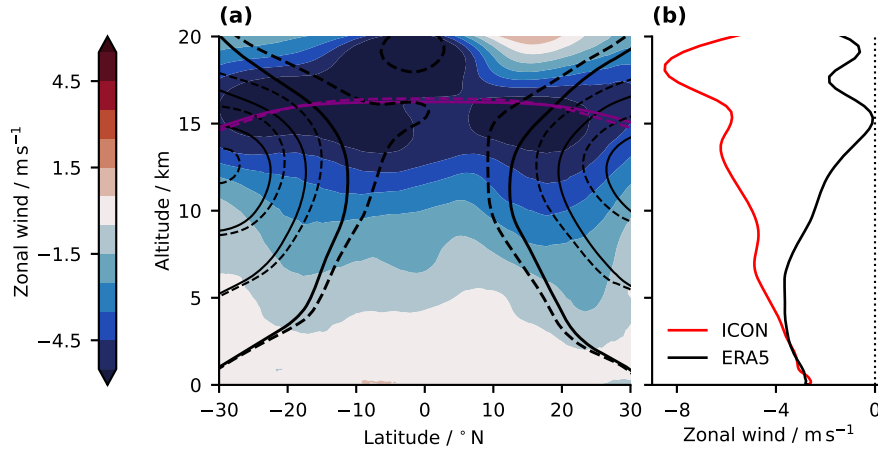


Figure 13. (a) Latitude-altitude cross section of the zonal mean zonal wind difference between the ICON simulation and the ERA5 reanalysis, averaged over the period April 01, 2004–March 31, 2006. Solid and dashed black contours indicate the zonal mean zonal wind in intervals of 10 m s^{-1} starting at 0 m s^{-1} (bold contours) of the ICON simulation and the ERA5 reanalysis, respectively. Solid and dashed purple contours mark the 370 K-isentrope, which is a proxy for the tropopause altitude, for the ICON simulation and the ERA5 reanalysis, respectively. (b) $10^\circ \text{ S}–10^\circ \text{ N}$ mean zonal wind in the ICON simulation and the ERA5 reanalysis as a function of altitude.

769 Figure 14a-c shows that the ICON simulation reproduces the basic qualitative aspects of the observed tropical precipitation spectrum reasonably well. The spectra of ICON, 770 IMERG, and ERA5 are all red in zonal wavenumber and frequency, but the spectrum 771 of the ICON simulation is slightly smoother than those of IMERG and ERA5. The ICON 772 simulation also shows a clear preference for westward propagating tropical waves, in agree- 773 ment with IMERG and ERA5. The spectra of the ICON simulation and IMERG both 774 organize along the same lines of constant zonal phase speed, i.e. $|c| = 15 \text{ m s}^{-1}$, while 775 the spectrum of ERA5 organizes along lines of constant absolute phase speed of slightly 776 more than 15 m s^{-1} . 777

778 Quantitatively, however, the precipitation spectra differ substantially between the 779 ICON simulation on the one hand and IMERG and ERA5 on the other. The ICON sim- 780 ulation substantially underestimates the tropical precipitation variance compared to IMERG, 781 over a wide spectral range of about $|k| < 130$ and $\omega < 2 \text{ cpd}$ (see white dashed lines 782 in Figure 14a,b). Only for larger wavenumbers and frequencies, the ICON simulation has 783 a slightly larger precipitation variance than IMERG, probably due to its higher native 784 spatial and temporal resolution compared to the IMERG data. Compared to the ERA5 785 reanalysis, the ICON simulation has a larger tropical precipitation variance in most parts 786 of the spectrum, except for the planetary-scale part, i.e. $|k| \leq 18$ and $\omega < 0.5 \text{ cpd}$, where 787 the tropical precipitation variance is still underestimated in ICON. The fact that the ICON 788 simulation has a larger precipitation variance than the ERA5 reanalysis, except for the 789 planetary-scale part of the spectrum, is due to the fact that ICON explicitly simulates 790 deep convection, while ERA5 parameterizes it. The parameterization of deep convection 791 has been shown to lead to an underestimation of high-frequency precipitation variance 792 compared to observations (e.g., J.-E. Kim & Alexander, 2013). The underestimation of 793 planetary-scale precipitation variance in the ICON simulation compared to the ERA5 794 reanalysis is also not surprising, since planetary-scale precipitation features in ERA5 —

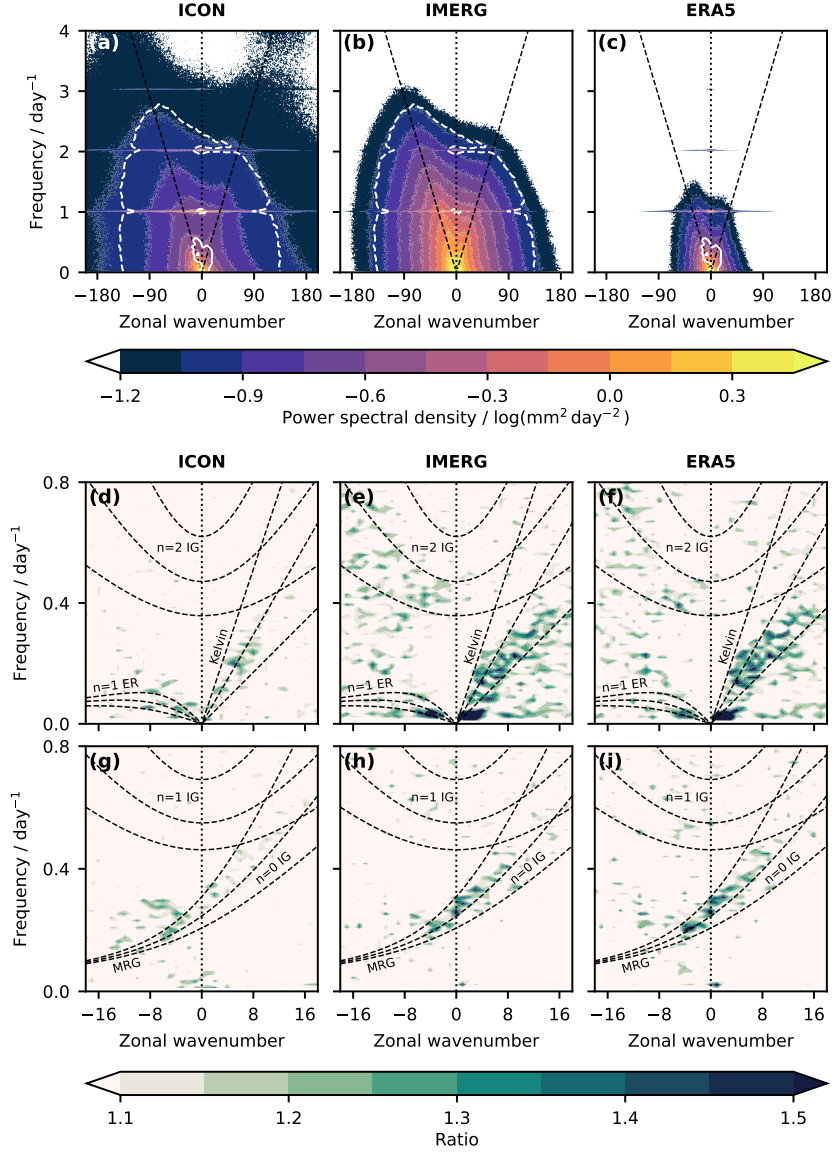


Figure 14. 15° S–15° N mean zonal wavenumber-frequency spectra of precipitation variance for (a) the ICON simulation, (b) the observational dataset IMERG, and (c) the ERA5 reanalysis, averaged over 29 tapered 92-day windows with a 34-day overlap. White lines in panels (a-c) indicate isolines where the smoothed power spectral density of ICON agrees with (dashed) IMERG and (solid) ERA5. Black dashed lines in panels (a-c) mark a constant ground-based zonal phase speed of $c = 15 \text{ m s}^{-1}$. Panels (d-f) and (g-i) show the 15° S–15° N mean zonal wavenumber-frequency spectra of normalized symmetric and antisymmetric precipitation variance, respectively, for (d,g) the ICON simulation, (e,h) IMERG, and (f,i) ERA5, averaged over 29 92-day windows with a 34-day overlap. The normalization has been performed according to Wheeler and Kiladis (1999). Black dashed lines in (d-i) mark ground-based theoretical dispersion curves of selected convectively coupled equatorial waves (CCEWs) with an equivalent depth h_e of 10 m, 30 m, and 90 m. Please note the following abbreviations: ER, Equatorial Rossby wave; IG, Inertia-gravity wave; and MRG, Mixed Rossby-gravity wave.

795 although precipitation is a pure model product — are still well constrained by observa-
796 tions and thus, by definition, close to IMERG.

797 In general, planetary-scale precipitation variance in the tropics is dominated by CCEWs,
798 which we will analyze in the following using the methodology of Wheeler and Kiladis (1999).
799 Therefore, we computed the zonal wavenumber-frequency spectra of the symmetric and
800 antisymmetric components of tropical precipitation (see Sec. 2.3.1 for details) for the same
801 29 tapered 92-day windows with a 34-day overlap that we computed the raw spectra for.
802 Afterwards, we normalized the symmetric and antisymmetric spectra by dividing them
803 by a smoothed background spectrum to highlight spectral peaks representing CCEWs.
804 We then averaged these spectra over all 29 windows and between 15° S and 15° N, and
805 the averaged spectra are shown in Figure 14d-j.

806 The normalized symmetric and antisymmetric spectra of the observational dataset
807 IMERG and the ERA5 reanalysis are nearly identical. This can be explained by the good
808 observational constraint on planetary-scale precipitation in ERA5. Both IMERG and
809 ERA5 have a rich spectrum of symmetric and antisymmetric CCEWs, including equa-
810 torial Kelvin waves, long $n = 0$ equatorial Rossby waves, mixed Rossby-gravity waves,
811 and $n = 0$ and $n = 2$ inertia-gravity waves. In contrast, the ICON simulation shows
812 much less organization of precipitation into CCEWs than IMERG and ERA5. The ICON
813 simulation has only weak signals of equatorial Kelvin waves, long $n = 0$ equatorial Rossby
814 waves, and mixed Rossby-gravity waves. The signals of $n = 0$ and $n = 2$ inertia-gravity
815 waves are practically absent, and the ICON simulation also shows no signal of the Madden-
816 Julian oscillation (MJO). The latter is in stark contrast to IMERG and ERA5, where
817 the MJO appears as a distinct spectral peak in the symmetric spectrum at $1 \leq k \leq$
818 3 and $\omega < 0.05$ cpd.

819 To conclude, the ICON simulation suffers from a substantial lack of CCEWs in com-
820 bination with a general underestimation of spectral precipitation variance compared to
821 the observational dataset IMERG. CCEWs are usually closely coupled to SEWs (Kawatani
822 et al., 2009; Maury et al., 2013) that ultimately drive the QBO, and more generally, the
823 spectral characteristics of the tropical precipitation variance have been shown to con-
824 trol the wave momentum fluxes in the lower tropical stratosphere (Ricciardulli & Gar-
825 cia, 2000; Horinouchi et al., 2003). Therefore, we conclude that the substantial under-
826 estimation of CCEWs in the ICON simulation is likely the root cause of the lack of planetary-
827 scale vertical wave momentum flux entering the lowermost stratosphere and, ultimately,
828 the lack of downward propagation of the ICON-QBO.

829 6 Discussion

830 6.1 Answers to the research questions

831 By performing a two-year-long simulation with the GSRM ICON with a horizon-
832 tal resolution of ~ 5 km and a vertical resolution between ~ 350 m and ~ 560 m in the strato-
833 sphere, we addressed the following research questions:

- 834 1. *Is a state-of-the-art GSRM capable of directly simulating a full cycle of the QBO*
835 *in a reasonable way? Which aspects of the QBO are well captured and which are*
836 *not?*

837 No, the current configuration of the state-of-the-art GSRM ICON is not yet ca-
838 pable of reasonably simulating a full QBO cycle. However, ICON does maintain
839 a QBO-like zonal wind structure in the tropical stratosphere throughout the whole
840 simulation. This is already a major achievement, given that a westerly — i.e. super-
841 rotational — jet at the equator can only be sustained by QBO-like vertical wave
842 forcing, and the ICON configuration employed was not specifically optimized for
843 this purpose. Furthermore, especially during the first year of the simulation, the

844 representation of the ICON-QBO in the upper QBO domain (i.e., between 25 km
 845 and 35 km) is in good agreement with the ERA5-QBO. Here, both the magnitude
 846 of the jets of the ICON-QBO and the rate of downward propagation of the ICON-
 847 QBO are reasonably well represented in the ICON simulation. In the lowermost
 848 stratosphere (i.e., below 25 km), however, the ICON-QBO suffers from a pronounced
 849 lack of downward propagation right from the beginning of the simulation. Dur-
 850 ing the second year of the simulation, the downward propagation of the ICON-
 851 QBO stops completely, and the ICON-QBO also suffers from too shallow and too
 852 weak jets.

853 2. *Why does the model simulate the QBO the way it does?*

854 *If the QBO is reasonably simulated, how is it forced in the simulation? Is it rea-*
 855 *sonable for the right reasons, or is it the product of compensating errors?*

856 *If the QBO is not reasonably simulated, what are the sources of QBO biases? Are*
 857 *QBO biases caused by biases in other aspects of the simulation?*

858 The reasonable downward propagation of the ICON-QBO in the upper QBO do-
 859 main (i.e., between 25 km and 35 km) is the product of an overall reasonable QBO
 860 momentum budget. Both the total QBO wave forcing and the residual advection
 861 of zonal momentum have a magnitude comparable to that of the ERA5 reanal-
 862 ysis. This implies that the downward propagation of the ICON-QBO in the up-
 863 per QBO domain in the first year of the ICON simulation occurs for the right rea-
 864 sons and is not the consequence of compensating errors. However, the contribu-
 865 tion of the meridional wave forcing to the total wave forcing is about twice as large
 866 in the ICON simulation as in the ERA5 reanalysis. In the lowermost stratosphere
 867 (i.e., below 25 km), the lack of downward propagation of the westerly jet of the
 868 ICON-QBO is due to a substantial underestimation of the vertical wave momen-
 869 tum flux entering the lower stratosphere, especially at planetary scales. We at-
 870 tribute this underestimation of the wave momentum flux entering the stratosphere
 871 to an underestimation of tropical precipitation variability in general and a pro-
 872 nounced lack of CCEWs in particular. The lack of downward propagation of the
 873 upper easterly jet of the ICON-QBO in the second year of the simulation may also
 874 be due to the filtering of slow westward propagating waves by an upper-tropospheric
 875 easterly bias in the ICON simulation.

876 **6.2 Direct QBO simulations in a GSRM: What have we learned, where**
 877 **do we stand?**

878 The overall reasonable representation of QBO dynamics in the easterly shear zone
 879 of the ICON-QBO between 25 km and 35 km during the first year of the simulation is
 880 a promising result. Since the downward propagation of the QBO easterly shear zone is
 881 mainly driven by GWs (see Anstey et al., 2022, and references therein), we take it as an
 882 indirect indication that a horizontal resolution of ~ 5 km is sufficient to resolve the GW
 883 spectrum relevant for driving the QBO. This is consistent with the results of Polichtchouk
 884 et al. (2021), who showed that the total resolved tropical GWMF in simulations with
 885 a horizontal grid spacing of $\mathcal{O}(10 \text{ km})$ – $\mathcal{O}(1 \text{ km})$ is nearly independent of horizontal res-
 886 olution and thus may be already converged. However, Polichtchouk et al. (2021) also showed
 887 that the partitioning of the tropical GWMF to zonal wavelengths still depends on the
 888 horizontal resolution, with the GWMF shifting to shorter zonal wavelengths at higher
 889 resolutions. Therefore, our results do not allow the conclusion that GWs that are not
 890 effectively resolved in our model configuration, i.e. GWs with horizontal wavelengths less
 891 than 60 km (see Stephan et al., 2019), are irrelevant for driving the QBO in reality.

892 Furthermore, our results suggest that the wave forcing by meridionally propagat-
 893 ing waves may be important for the QBO, at least in the upper QBO domain. Here, the
 894 meridional wave forcing contributes about $\sim 25\%$ to the total wave forcing of the ICON-
 895 QBO (see Fig. 5a). In contrast, the meridional wave forcing contributes only 10%–15%
 896 to the total wave forcing in the same altitude range in the ERA5 reanalysis. We spec-

897 ulate that the difference between ICON and ERA5 is mainly due to meridionally prop-
 898 agating GWs in the ICON simulation, which are not resolved in the ERA5 reanalysis.
 899 This finding would support recent findings of Y.-H. Kim et al. (2023), who suggest that
 900 oblique GW propagation plays a crucial role in QBO dynamics based on results from a
 901 novel GW parameterization that allows oblique GW propagation (e.g., Bölöni et al., 2021;
 902 Y.-H. Kim et al., 2021). Taking into account that most GW parameterizations do not
 903 account for meridional GW propagation, this would also imply that the QBO momen-
 904 tum budgets in conventional GCMs employing simple GW parameterizations may be bi-
 905 ased towards too strong vertical wave forcing.

906 The main bias of the ICON-QBO is a substantial lack of downward propagation
 907 in the lowermost stratosphere, which is the result of an underestimation of the vertical
 908 wave forcing, primarily at the planetary scale. We have attributed this underestimation
 909 of planetary-scale wave forcing to a pronounced lack of CCEWs in the tropical tropo-
 910 sphere. However, the root cause of the lack of CCEWs and, more generally, the misrep-
 911 resentation of spatio-temporal variability of tropical deep convection across scales is un-
 912 clear. Takasuka et al. (2024) showed that careful and targeted tuning of the remaining
 913 major parameterizations of a GSRM — that is, the parameterizations of cloud micro-
 914 physics and turbulent mixing — can greatly improve the model’s representation of tropi-
 915 cal deep convection on a variety of spatio-temporal scales. Therefore, it seems plausi-
 916 ble that an analog tuning approach in the present ICON configuration may help to achieve
 917 a more realistic representation of the spatio-temporal variability of tropical deep con-
 918 vection, including CCEWs. On the other hand, the lack of CCEWs and spatio-temporal
 919 variability of tropical convection may be related to the employed horizontal resolution
 920 of ~ 5 km, which is in the convective gray zone and thus should be considered ”convection-
 921 permitting” rather than ”convection-resolving” (e.g., Prein et al., 2015). GSRMs oper-
 922 ating in the gray zone have been shown to produce convective cells that are too small
 923 and too intense, preventing convective organization into larger and more long-lived or-
 924 ganized convective systems (Crook et al., 2019; Becker et al., 2021). We speculate that
 925 this may also hinder the formation of CCEWs and the MJO, implying that a GSRM in
 926 the gray zone may still be too coarse to explicitly resolve the generation of the full wave
 927 spectrum necessary to drive the QBO in the lowermost stratosphere.

928 At this point, it should also be mentioned that the CCEWs in the ICON simula-
 929 tion are indeed weak, but not extraordinarily weak compared to conventional GCMs, such
 930 as those which participated in QBOi (see Fig. 2 of Holt et al., 2020). However, unlike the
 931 ICON simulation, the QBOi models simulated a reasonable QBO regardless of their weak
 932 CCEWs (Bushell et al., 2020). This is because conventional GCMs can compensate for
 933 potential biases in their resolved wave forcing via their GW parameterization, a tuning
 934 option GSRMs no longer have. This has further implications: first, it suggests that the
 935 simulated QBO in conventional GCMs is often the product of compensating errors, and
 936 their QBO momentum budget is rather arbitrary. Second, it implies that a realistic rep-
 937 resentation of the mean state and the variability of the tropical troposphere is crucial
 938 for a realistic representation of the QBO in GSRMs, probably even more so than in con-
 939 ventional GCMs.

940 Interestingly, a lack of downward propagation of the QBO to the tropopause and
 941 a too weak QBO amplitude in the lowermost stratosphere is also a common bias in con-
 942 ventional GCMs (Schenzinger et al., 2017; Bushell et al., 2020; Anstey et al., 2022). In
 943 these models, the bias is typically attributed to an insufficient vertical resolution, which
 944 does not adequately resolve the vertical propagation and wave-mean flow interactions
 945 of waves with small vertical wavelengths, especially planetary-scale Kelvin waves (Boville
 946 & Randel, 1992; Giorgetta et al., 2006; Anstey et al., 2016; Geller et al., 2016; Garfinkel
 947 et al., 2022). The vertical resolution of the ICON configuration employed (i.e., 350 m to
 948 560 m in the stratosphere) is usually considered sufficient in this regard, and indeed the
 949 vertical propagation and damping of Kelvin waves is represented reasonably in the ICON

simulation (see Fig. 11). However, as suggested by Bramberger et al. (2022), eastward-propagating inertia-gravity waves with large horizontal but very short vertical wavelengths (i.e., < 1 km) may also contribute substantially to driving the downward propagation of the QBO in the lowermost stratosphere. The vertical resolution of the ICON configuration employed is still too coarse to resolve these waves. In addition, Skamarock et al. (2019) showed that resolved flow features in the free atmosphere, especially mesoscale GWs, converge only at vertical grid spacings of ≤ 200 m. This suggests that the vertical resolution in the ICON configuration employed may still be too coarse to resolve the full QBO wave forcing.

A general limitation of our findings is that they are based on a relatively short simulation, which further is only representative of one specific QBO phase. Some of our results are based on an even shorter analysis period of less than five months. While we do not think that this limitations impact our key results, longer simulations are desirable to achieve statistically more robust results.

7 Summary and prospects

In this study, we present the first attempt at a direct simulation of a full QBO cycle in a GSRM, employing neither a parameterization of deep convection nor GWs. This means that, for the first time, the generation, propagation, and dissipation of the entire wave spectrum driving a QBO in a model is resolved explicitly and thus in a physically meaningful way. For the simulation in this study, we used the state-of-the-art GSRM ICON. Although the details of the QBO-like winds simulated in ICON do not agree with the ERA5 reanalysis — as is to be expected for such a first-of-its-kind simulation — the overall results of the simulation are encouraging. The ICON simulation reproduced the basic zonal momentum budget in the QBO easterly shear zone between 25 km–35 km during the first boreal summer of the simulation with a high degree of fidelity. This indicates that a GSRM with a horizontal grid spacing of $\mathcal{O}(5$ km) basically resolves the relevant processes that drive the QBO in this altitude range, in particular its wave-driving by GWs. Furthermore, we were able to attribute the biases in the simulated QBO to biases in the tropical troposphere, namely an underestimation of the spatio-temporal variability of tropical convection and CCEWs, and excessive wave filtering by an upper-tropospheric easterly zonal wind bias. These results suggest that the realistic representation of the tropical troposphere, in particular the spatio-temporal variability of tropical convection across scales, is currently the biggest roadblock of a successful representation of the QBO in GSRMs — at least in the present one. In contrast, the propagation and dissipation of the wave spectrum relevant for the QBO in the stratosphere do not seem to be a major problem.

Given the current advances in exascale computing, the ICON configuration employed may soon realistically reach a throughput of ~ 1 SYPD, putting multi-decadal global storm-resolving simulations of the QBO within reach (see Sec. 6.5 of Giorgetta et al., 2022). Direct simulations of a full QBO cycle at horizontal grid spacings close to 1 km or vertical grid spacings of ~ 100 m throughout the stratosphere also seem computationally plausible (cmp. Neumann et al., 2019). Such simulations have great potential to advance our understanding of the QBO and to resolve long-standing problems, such as the inability of conventional GCMs to reproduce the observed connection between the QBO and the MJO (Martin et al., 2021) or the large uncertainty in the possible response of the QBO to global warming (Richter, Butchart, et al., 2020). Our goal of being able to exploit this exciting technological potential with ICON places clear demands on future work. First and foremost, we need to achieve a realistic representation of CCEWs in ICON — this is the necessary groundwork. Afterwards, more detailed sensitivity studies of the QBO with respect to the parameter setting of ICON would help to understand the stringent requirements for a reasonable representation of the QBO in a GSRM. Given this roadmap

1001 for future work, accompanied by the concurrently growing technological capabilities, we
 1002 are optimistic that we will soon achieve the first realistic simulation of the QBO in a GSRM.

1003 **Open Research Section**

1004 The version of the ICON code used to run the simulation analyzed in this study,
 1005 as well as the boundary fields for the simulation are available at the data repository Ed-
 1006 mond (Franke, 2024). Detailed information on the ICON model are provided by DWD
 1007 (2024). The ERA5 reanalysis data used for the analysis presented in this study was pro-
 1008 vided by the Copernicus Climate Change Service (C3S) Climate Data Store (CDS) at
 1009 the DKRZ (Hersbach et al., 2018b, 2018a). A detailed description of ERA5 is given by
 1010 (Hersbach et al., 2020). The IMERG precipitation data used for the analysis presented
 1011 in this study was supported by the Integrated Climate Data Center (ICDC), the Cen-
 1012 ter for Earth System Research and Sustainability (CEN), and the University of Ham-
 1013 burg (Huffman et al., 2022). All scripts used to process and analyze the model output
 1014 and the ERA5 and IMERG raw data are available at the data repository Edmond (Franke,
 1015 2024).

1016 **Acknowledgments**

1017 We would like to thank Dmitry Alexeev for assistance in porting the linearized Cariolle
 1018 ozone scheme to GPU architecture, and Carsten Beyer and Claudia Frauen for techni-
 1019 cal support in running the ICON simulation on the GPU partition of the supercomputer
 1020 Levante at the German Climate Computing Centre (Deutsches Klimarechenzentrum, DKRZ).
 1021 We also thank Sebastián Ortega for providing the basic Python libraries for computing
 1022 the TEM diagnostics and performing the spectral analysis, and Ulrike Niemeier and Hauke
 1023 Schmidt for valuable discussions at different stages of the manuscript. We acknowledge
 1024 the Integrated Climate Data Center (ICDC), the Center for Earth System Research and
 1025 Sustainability (CEN), and the University of Hamburg for supporting the IMERG data.
 1026 We further acknowledge the German Federal Ministry of Education and Research (BMBF)
 1027 for partial support through the program Role of the Middle Atmosphere in Climate (ROMIC
 1028 II: QUBICC).

1029 **References**

- 1030 Achatz, U., Alexander, M. J., Becker, E., Chun, H.-Y., Dörnbrack, A., Holt, L., ...
 1031 Wright, C. J. (2023). Atmospheric Gravity Waves: Processes and Parameteri-
 1032 zation. *Journal of the Atmospheric Sciences*. doi: 10.1175/JAS-D-23-0210.1
- 1033 Alexander, M. J., Geller, M., McLandress, C., Polavarapu, S., Preusse, P., Sassi,
 1034 F., ... Watanabe, S. (2010). Recent developments in gravity-wave effects in
 1035 climate models and the global distribution of gravity-wave momentum flux
 1036 from observations and models. *Quarterly Journal of the Royal Meteorological*
 1037 *Society*, 136(650), 1103–1124. doi: 10.1002/qj.637
- 1038 Andrews, D. G., & McIntyre, M. E. (1976). Planetary Waves in Horizontal and
 1039 Vertical Shear: The Generalized Eliassen-Palm Relation and the Mean Zonal
 1040 Acceleration. *Journal of the Atmospheric Sciences*, 33(11), 2031–2048. doi:
 1041 10.1175/1520-0469(1976)033<2031:PWIHAV>2.0.CO;2
- 1042 Anstey, J. A., Banyard, T. P., Butchart, N., Coy, L., Newman, P. A., Osprey, S.,
 1043 & Wright, C. J. (2021). Prospect of Increased Disruption to the QBO in a
 1044 Changing Climate. *Geophysical Research Letters*, 48(15), e2021GL093058. doi:
 1045 10.1029/2021GL093058
- 1046 Anstey, J. A., Osprey, S. M., Alexander, J., Baldwin, M. P., Butchart, N., Gray, L.,
 1047 ... Richter, J. H. (2022). Impacts, processes and projections of the quasi-
 1048 biennial oscillation. *Nature Reviews Earth & Environment*, 3(9), 588–603. doi:
 1049 10.1038/s43017-022-00323-7

- 1050 Anstey, J. A., Scinocca, J. F., & Keller, M. (2016). Simulating the QBO in an
 1051 Atmospheric General Circulation Model: Sensitivity to Resolved and Paramete-
 1052 rized Forcing. *Journal of the Atmospheric Sciences*, *73*(4), 1649–1665. doi:
 1053 10.1175/JAS-D-15-0099.1
- 1054 Baldauf, M., Seifert, A., Förstner, J., Majewski, D., Raschendorfer, M., & Rein-
 1055 hardt, T. (2011). Operational convective-scale numerical weather prediction
 1056 with the cosmo model: Description and sensitivities. *Monthly Weather Review*,
 1057 *139*(12), 3887–3905. doi: 10.1175/MWR-D-10-05013.1
- 1058 Baldwin, M. P., Gray, L. J., Dunkerton, T. J., Hamilton, K., Haynes, P. H., Randel,
 1059 W. J., ... Takahashi, M. (2001). The quasi-biennial oscillation. *Reviews of*
 1060 *Geophysics*, *39*(2), 179–229. doi: 10.1029/1999RG000073
- 1061 Becker, T., Bechtold, P., & Sandu, I. (2021). Characteristics of convective precipita-
 1062 tion over tropical Africa in storm-resolving global simulations. *Quarterly Jour-
 1063 nal of the Royal Meteorological Society*, *147*(741), 4388–4407. doi: 10.1002/qj
 1064 .4185
- 1065 Beres, J. H., Alexander, M. J., & Holton, J. R. (2004). A Method of Specifying the
 1066 Gravity Wave Spectrum above Convection Based on Latent Heating Properties
 1067 and Background Wind. *Journal of the Atmospheric Sciences*, *61*(3), 324–337.
 1068 doi: 10.1175/1520-0469(2004)061<0324:AMOSTG>2.0.CO;2
- 1069 Boville, B. A., & Randel, W. J. (1992). Equatorial Waves in a Stratospheric GCM:
 1070 Effects of Vertical Resolution. *Journal of Atmospheric Sciences*, *49*(9), 785–
 1071 801. doi: 10.1175/1520-0469(1992)049<0785:EWIASG>2.0.CO;2
- 1072 Bramberger, M., Alexander, M. J., Davis, S., Podglajen, A., Hertzog, A., Kalnajs,
 1073 L., ... Khaykin, S. (2022). First Super-Pressure Balloon-Borne Fine-Vertical-
 1074 Scale Profiles in the Upper TTL: Impacts of Atmospheric Waves on Cirrus
 1075 Clouds and the QBO. *Geophysical Research Letters*, *49*(5), e2021GL097596.
 1076 doi: 10.1029/2021GL097596
- 1077 Bushell, A. C., Anstey, J. A., Butchart, N., Kawatani, Y., Osprey, S. M., Richter,
 1078 J. H., ... Yukimoto, S. (2020). Evaluation of the Quasi-Biennial Oscillation in
 1079 global climate models for the SPARC QBO-initiative. *Quarterly Journal of the*
 1080 *Royal Meteorological Society*, *148*(744), 1459–1489. doi: 10.1002/qj.3765
- 1081 Bushell, A. C., Butchart, N., Derbyshire, S. H., Jackson, D. R., Shutts, G. J.,
 1082 Vosper, S. B., & Webster, S. (2015). Parameterized Gravity Wave Momen-
 1083 tum Fluxes from Sources Related to Convection and Large-Scale Precipitation
 1084 Processes in a Global Atmosphere Model. *Journal of the Atmospheric Sci-
 1085 ences*, *72*(11), 4349–4371. doi: 10.1175/JAS-D-15-0022.1
- 1086 Butchart, N., Anstey, J. A., Hamilton, K., Osprey, S., McLandress, C., Bushell,
 1087 A. C., ... Yukimoto, S. (2018). Overview of experiment design and compar-
 1088 ison of models participating in phase 1 of the SPARC Quasi-Biennial Oscilla-
 1089 tion initiative (QBOi). *Geoscientific Model Development*, *11*(3), 1009–1032.
 1090 doi: 10.5194/gmd-11-1009-2018
- 1091 Bölöni, G., Kim, Y.-H., Borchert, S., & Achatz, U. (2021). Toward Transient
 1092 Subgrid-Scale Gravity Wave Representation in Atmospheric Models. Part
 1093 I: Propagation Model Including Nondissipative Wave-Mean-Flow Inter-
 1094 actions. *Journal of the Atmospheric Sciences*, *78*(4), 1317–1338. doi:
 1095 10.1175/JAS-D-20-0065.1
- 1096 Cariolle, D., & Teyssède, H. (2007). A revised linear ozone photochemistry param-
 1097 eterization for use in transport and general circulation models: multi-annual
 1098 simulations. *Atmospheric Chemistry and Physics*, *7*(9), 2183–2196. doi:
 1099 10.5194/acp-7-2183-2007
- 1100 Crook, J., Klein, C., Folwell, S., Taylor, C. M., Parker, D. J., Stratton, R., & Stein,
 1101 T. (2019). Assessment of the representation of west african storm lifecycles in
 1102 convection-permitting simulations. *Earth and Space Science*, *6*(5), 818–835.
 1103 doi: 10.1029/2018EA000491
- 1104 Doms, G., Förstner, J., Heise, E., Herzog, H.-J., Mironov, D., Raschendorfer, M.,

- 1105 ... Vogel, G. (2021). *Cosmo-model version 6.00: A description of the*
 1106 *nonhydrostatic regional cosmo-model - part ii: Physical parametrizations*
 1107 (Tech. Rep.). Deutscher Wetterdienst. (last access: October 11, 2023) doi:
 1108 10.5676/DWD_PUB/NWV/COSMO-DOC.6.00-II
- 1109 Durack, P. J., & Taylor, K. E. (2019). *PCMDI AMIP SST and sea-ice boundary*
 1110 *conditions version 1.1.6 [Dataset]*. Earth System Grid Federation. doi: 10
 1111 .22033/ESGF/input4MIPs.12381
- 1112 DWD. (2024). *Icon model*. Retrieved 2024-02-26, from [https://www.icon-model](https://www.icon-model.org)
 1113 [.org](https://www.icon-model.org)
- 1114 Fels, S. B. (1982). A Parameterization of Scale-Dependent Radiative Damping
 1115 Rates in the Middle Atmosphere. *Journal of Atmospheric Sciences*, *39*(5),
 1116 1141–1152. doi: 10.1175/1520-0469(1982)039<1141:APOSDR>2.0.CO;2
- 1117 Franke, H. (2024). *Towards the direct simulation of the quasi-biennial oscillation in*
 1118 *a global storm-resolving model (Version 1) [Dataset]*. Edmond. doi: 10.17617/
 1119 3.A4LJEB
- 1120 Franke, H., Preusse, P., & Giorgetta, M. (2023). Changes of tropical gravity waves
 1121 and the quasi-biennial oscillation in storm-resolving simulations of idealized
 1122 global warming. *Quarterly Journal of the Royal Meteorological Society*,
 1123 *149*(756), 2838–2860. doi: 10.1002/qj.4534
- 1124 Frierson, D. M. W., Kim, D., Kang, I.-S., Lee, M.-I., & Lin, J. (2011). Structure
 1125 of AGCM-Simulated Convectively Coupled Kelvin Waves and Sensitivity to
 1126 Convective Parameterization. *Journal of the Atmospheric Sciences*, *68*(1),
 1127 26–45. doi: 10.1175/2010JAS3356.1
- 1128 Fritts, D. C., & Alexander, M. J. (2003). Gravity wave dynamics and ef-
 1129 fects in the middle atmosphere. *Reviews of Geophysics*, *41*(1003). doi:
 1130 10.1029/2001rg000106
- 1131 Garfinkel, C. I., Gerber, E. P., Shamir, O., Rao, J., Jucker, M., White, I., & Paldor,
 1132 N. (2022). A QBO cookbook: Sensitivity of the Quasi-Biennial Oscilla-
 1133 tion to resolution, resolved waves, and parameterized gravity waves. *Jour-
 1134 nal of Advances in Modeling Earth Systems*, *14*(3), e2021MS002568. doi:
 1135 10.1029/2021MS002568
- 1136 Geller, M. A., Zhou, T., Shindell, D., Ruedy, R., Aleinov, I., Nazarenko, L., ...
 1137 Faluvegi, G. (2016). Modeling the QBO—Improvements resulting from higher-
 1138 model vertical resolution. *Journal of Advances in Modeling Earth Systems*,
 1139 *8*(3), 1092–1105. doi: 10.1002/2016MS000699
- 1140 Giorgetta, M. A., Brokopf, R., Crueger, T., Esch, M., Fiedler, S., Helmert, J., ...
 1141 Stevens, B. (2018). ICON-A, the Atmosphere Component of the ICON Earth
 1142 System Model: I. Model Description. *Journal of Advances in Modeling Earth*
 1143 *Systems*, *10*(7), 1613–1637. doi: 10.1029/2017ms001242
- 1144 Giorgetta, M. A., Manzini, E., Roeckner, E., Esch, M., & Bengtsson, L. (2006).
 1145 Climatology and Forcing of the Quasi-Biennial Oscillation in the MAECHAM5
 1146 Model. *Journal of Climate*, *19*(16), 3882–3901. doi: 10.1175/JCLI3830.1
- 1147 Giorgetta, M. A., Sawyer, W., Lapillonne, X., Adamidis, P., Alexeev, D., Clément,
 1148 V., ... Stevens, B. (2022). The ICON-A model for direct QBO simulations on
 1149 GPUs (version icon-cscs:baf28a514). *Geoscientific Model Development*, *15*(18),
 1150 6985–7016. doi: 10.5194/gmd-15-6985-2022
- 1151 Hardiman, S. C., Andrews, D. G., White, A. A., Butchart, N., & Edmond, I. (2010).
 1152 Using Different Formulations of the Transformed Eulerian Mean Equations
 1153 and Eliassen–Palm Diagnostics in General Circulation Models. *Journal of the*
 1154 *Atmospheric Sciences*, *67*(6), 1983–1995. doi: 10.1175/2010JAS3355.1
- 1155 Hersbach, H., Bell, B., Berrisford, P., Biavati, G., Horányi, A., Muñoz Sabater, J.,
 1156 ... Thépaut, J.-N. (2018a). *ERA5 hourly data on pressure levels from 1979*
 1157 *to present [Dataset]*. Copernicus Climate Change Service (C3S) Climate Data
 1158 Store (CDS). (Accessed at DKRZ on 10/13/2023) doi: 10.24381/cds.bd0915c6
- 1159 Hersbach, H., Bell, B., Berrisford, P., Biavati, G., Horányi, A., Muñoz Sabater, J.,

- 1160 ... Thépaut, J.-N. (2018b). *ERA5 hourly data on single levels from 1979 to*
 1161 *present [Dataset]*. Copernicus Climate Change Service (C3S) Climate Data
 1162 Store (CDS). (Accessed at DKRZ on 10/13/2023) doi: 10.24381/cds.adbb2d47
- 1163 Hersbach, H., Bell, B., Berrisford, P., Hirahara, S., Horányi, A., Muñoz-Sabater, J.,
 1164 ... Thépaut, J.-N. (2020). The ERA5 global reanalysis. *Quarterly Journal of*
 1165 *the Royal Meteorological Society*, 146(730), 1999–2049. doi: 10.1002/qj.3803
- 1166 Holt, L. A., Lott, F., Garcia, R. R., Kiladis, G. N., Cheng, Y.-M., Anstey, J. A.,
 1167 ... Yukimoto, S. (2020). An evaluation of tropical waves and wave forcing of
 1168 the QBO in the QBOi models. *Quarterly Journal of the Royal Meteorological*
 1169 *Society*, 148(744), 1541–1567. doi: 10.1002/qj.3827
- 1170 Holton, J. R. (1972). Waves in the Equatorial Stratosphere Generated by Tropo-
 1171 spheric Heat Sources. *Journal of Atmospheric Sciences*, 29(2), 368–375. doi:
 1172 10.1175/1520-0469(1972)029<0368:WITESG>2.0.CO;2
- 1173 Horinouchi, T., Pawson, S., Shibata, K., Langematz, U., Manzini, E., Giorgetta,
 1174 M. A., ... Scaife, A. A. (2003). Tropical Cumulus Convection and Upward-
 1175 Propagating Waves in Middle-Atmospheric GCMs. *Journal of the Atmo-*
 1176 *spheric Sciences*, 60(22), 2765–2782. doi: 10.1175/1520-0469(2003)060<2765:
 1177 TCCAUW>2.0.CO;2
- 1178 Huffman, G., Stocker, E., Bolvin, D., Nelkin, E., & Tan, J. (2022). *GPM IMERG*
 1179 *Final Precipitation L3 Half Hourly 0.1 degree x 0.1 degree V06 [Dataset]*.
 1180 Goddard Earth Sciences Data and Information Services Center (GES DISC).
 1181 (Accessed on 10/06/2023, distributed in netCDF file format by ICDC, CEN,
 1182 University of Hamburg) doi: 10.5067/GPM/IMERG/3B-HH/06
- 1183 Kawatani, Y., Takahashi, M., Sato, K., Alexander, S. P., & Tsuda, T. (2009).
 1184 Global distribution of atmospheric waves in the equatorial upper tropo-
 1185 sphere and lower stratosphere: AGCM simulation of sources and propaga-
 1186 tion. *Journal of Geophysical Research: Atmospheres*, 114(D01102). doi:
 1187 10.1029/2008JD010374
- 1188 Kim, J.-E., & Alexander, M. J. (2013). Tropical Precipitation Variability and
 1189 Convectively Coupled Equatorial Waves on Submonthly Time Scales in
 1190 Reanalyses and TRMM. *Journal of Climate*, 26(10), 3013 - 3030. doi:
 1191 10.1175/JCLI-D-12-00353.1
- 1192 Kim, Y.-H., Bölöni, G., Borchert, S., Chun, H.-Y., & Achatz, U. (2021). Toward
 1193 Transient Subgrid-Scale Gravity Wave Representation in Atmospheric Models.
 1194 Part II: Wave Intermittency Simulated with Convective Sources. *Journal of the*
 1195 *Atmospheric Sciences*, 78(4), 1339–1357. doi: 10.1175/JAS-D-20-0066.1
- 1196 Kim, Y.-H., Voelker, G. S., Bölöni, G., Zängl, G., & Achatz, U. (2023). Crucial
 1197 role of obliquely propagating gravity waves in the quasi-biennial oscillation
 1198 dynamics. *EGU sphere*, 2023, 1–18. doi: 10.5194/egusphere-2023-2663
- 1199 Kinne, S., O’Donnell, D., Stier, P., Kloster, S., Zhang, K., Schmidt, H., ... Stevens,
 1200 B. (2013). Mac-v1: A new global aerosol climatology for climate stud-
 1201 ies. *Journal of Advances in Modeling Earth Systems*, 5(4), 704–740. doi:
 1202 10.1002/jame.20035
- 1203 Kirchner, J. W. (2005). Aliasing in $1/f^\alpha$ noise spectra: Origins, consequences, and
 1204 remedies. *Physical Review E*, 71(6). doi: 10.1103/physreve.71.066110
- 1205 Klemp, J. B., Dudhia, J., & Hassiotis, A. D. (2008). An Upper Gravity-Wave
 1206 Absorbing Layer for NWP Applications. *Monthly Weather Review*, 136(10),
 1207 3987–4004. doi: 10.1175/2008MWR2596.1
- 1208 Krismer, T. R., & Giorgetta, M. A. (2014). Wave Forcing of the Quasi-Biennial Os-
 1209 cillation in the Max Planck Institute Earth System Model. *Journal of the At-*
 1210 *mospheric Sciences*, 71(6), 1985–2006. doi: 10.1175/JAS-D-13-0310.1
- 1211 Krismer, T. R., Giorgetta, M. A., von Storch, J. S., & Fast, I. (2015). The Influe-
 1212 nce of the Spectral Truncation on the Simulation of Waves in the Tropical
 1213 Stratosphere. *Journal of the Atmospheric Sciences*, 72(10), 3819–3828. doi:
 1214 10.1175/JAS-D-14-0240.1

- 1215 Lin, J.-L., Lee, M.-I., Kim, D., Kang, I.-S., & Frierson, D. M. W. (2008). The
 1216 Impacts of Convective Parameterization and Moisture Triggering on AGCM-
 1217 Simulated Convectively Coupled Equatorial Waves. *Journal of Climate*, *21*(5),
 1218 883–909. doi: 10.1175/2007JCLI1790.1
- 1219 Martin, Z., Son, S.-W., Butler, A., Hendon, H., Kim, H., Sobel, A., . . . Zhang, C.
 1220 (2021). The influence of the quasi-biennial oscillation on the madden–julian
 1221 oscillation. *Nature Reviews Earth & Environment*, *2*(7), 477–489. doi:
 1222 10.1038/s43017-021-00173-9
- 1223 Mauritsen, T., Svensson, G., Zilitinkevich, S. S., Esau, I., Enger, L., & Grisogono,
 1224 B. (2007). A Total Turbulent Energy Closure Model for Neutrally and Stably
 1225 Stratified Atmospheric Boundary Layers. *Journal of the Atmospheric Sciences*,
 1226 *64*(11), 4113–4126. doi: 10.1175/2007JAS2294.1
- 1227 Maury, P., Lott, F., Guez, L., & Duvel, J.-P. (2013). Tropical variability and strato-
 1228 spheric equatorial waves in the IPSLCM5 model. *Climate Dynamics*, *40*(9–10),
 1229 2331–2344. doi: 10.1007/s00382-011-1273-0
- 1230 Meinshausen, M., Vogel, E., Nauels, A., Lorbacher, K., Meinshausen, N., Etheridge,
 1231 D. M., . . . Weiss, R. (2017). Historical greenhouse gas concentrations for cli-
 1232 mate modelling (CMIP6). *Geoscientific Model Development*, *10*(5), 2057–2116.
 1233 doi: 10.5194/gmd-10-2057-2017
- 1234 Neumann, P., Düben, P., Adamidis, P., Bauer, P., Brück, M., Kornbluh, L., . . .
 1235 Biercamp, J. (2019). Assessing the scales in numerical weather and climate
 1236 predictions: will exascale be the rescue? *Philosophical Transactions of the*
 1237 *Royal Society A: Mathematical, Physical and Engineering Sciences*, *377*(2142),
 1238 20180148. doi: 10.1098/rsta.2018.0148
- 1239 Osprey, S. M., Butchart, N., Knight, J. R., Scaife, A. A., Hamilton, K., Anstey,
 1240 J. A., . . . Zhang, C. (2016). An unexpected disruption of the atmo-
 1241 spheric quasi-biennial oscillation. *Science*, *353*(6306), 1424–1427. doi:
 1242 10.1126/science.aah4156
- 1243 Pahlavan, H. A., Fu, Q., Wallace, J. M., & Kiladis, G. N. (2021). Revisiting the
 1244 Quasi-Biennial Oscillation as Seen in ERA5. Part I: Description and Momen-
 1245 tum Budget. *Journal of the Atmospheric Sciences*, *78*(3), 673–691. doi:
 1246 10.1175/JAS-D-20-0248.1
- 1247 Pahlavan, H. A., Wallace, J. M., Fu, Q., & Kiladis, G. N. (2021). Revisiting the
 1248 Quasi-Biennial Oscillation as Seen in ERA5. Part II: Evaluation of Waves and
 1249 Wave Forcing. *Journal of the Atmospheric Sciences*, *78*(3), 693–707. doi:
 1250 10.1175/JAS-D-20-0249.1
- 1251 Pincus, R., Mlawer, E. J., & Delamere, J. S. (2019). Balancing Accuracy, Ef-
 1252 ficiency, and Flexibility in Radiation Calculations for Dynamical Mod-
 1253 els. *Journal of Advances in Modeling Earth Systems*, *11*, 3074–3089. doi:
 1254 10.1029/2019MS001621
- 1255 Pithan, F., Angevine, W., & Mauritsen, T. (2015). Improving a global model from
 1256 the boundary layer: Total turbulent energy and the neutral limit Prandtl num-
 1257 ber. *Journal of Advances in Modeling Earth Systems*, *7*(2), 791–805. doi:
 1258 10.1002/2014ms000382
- 1259 Plougonven, R., de la Cámara, A., Hertzog, A., & Lott, F. (2020). How does
 1260 knowledge of atmospheric gravity waves guide their parameterizations? *Quar-
 1261 terly Journal of the Royal Meteorological Society*, *146*(728), 1529–1543. doi:
 1262 10.1002/qj.3732
- 1263 Polichtchouk, I., Wedi, N., & Kim, Y.-H. (2021). Resolved gravity waves in the
 1264 tropical stratosphere: Impact of horizontal resolution and deep convection
 1265 parametrization. *Quarterly Journal of the Royal Meteorological Society*,
 1266 *148*(742), 233–251. doi: 10.1002/qj.4202
- 1267 Prein, A. F., Langhans, W., Fossler, G., Ferrone, A., Ban, N., Goergen, K., . . . Le-
 1268 ung, R. (2015). A review on regional convection-permitting climate modeling:
 1269 Demonstrations, prospects, and challenges. *Reviews of Geophysics*, *53*(2),

- 1270 323–361. doi: 10.1002/2014RG000475
- 1271 Ricciardulli, L., & Garcia, R. R. (2000). The Excitation of Equatorial Waves by
1272 Deep Convection in the NCAR Community Climate Model (CCM3). *Journal*
1273 *of the Atmospheric Sciences*, *57*(21), 3461–3487. doi: 10.1175/1520-0469(2000)
1274 057<3461:TEOEWB>2.0.CO;2
- 1275 Richter, J. H., Anstey, J. A., Butchart, N., Kawatani, Y., Meehl, G. A., Osprey, S.,
1276 & Simpson, I. R. (2020). Progress in Simulating the Quasi-Biennial Oscilla-
1277 tion in CMIP Models. *Journal of Geophysical Research: Atmospheres*, *125*(8),
1278 e2019JD032362. doi: 10.1029/2019JD032362
- 1279 Richter, J. H., Butchart, N., Kawatani, Y., Bushell, A. C., Holt, L., Serva, F., ...
1280 Yukimoto, S. (2020). Response of the Quasi-Biennial Oscillation to a warming
1281 climate in global climate models. *Quarterly Journal of the Royal Meteorological*
1282 *Society*, *148*(744), 1490–1518. doi: 10.1002/qj.3749
- 1283 Richter, J. H., Sassi, F., & Garcia, R. R. (2010). Toward a Physically Based Gravity
1284 Wave Source Parameterization in a General Circulation Model. *Journal of the*
1285 *Atmospheric Sciences*, *67*(1), 136–156. doi: 10.1175/2009JAS3112.1
- 1286 Salby, M. L., & Garcia, R. R. (1987). Transient Response to Localized Episodic
1287 Heating in the Tropics. Part I: Excitation and Short-Time Near-Field Be-
1288 havior. *Journal of Atmospheric Sciences*, *44*(2), 458–498. doi: 10.1175/
1289 1520-0469(1987)044<0458:TRTLEH>2.0.CO;2
- 1290 Satoh, M., Stevens, B., Judt, F., Khairoutdinov, M., Lin, S.-J., Putman, W. M., &
1291 Düben, P. (2019). Global Cloud-Resolving Models. *Current Climate Change*
1292 *Reports*, *5*(3), 172–184. doi: 10.1007/s40641-019-00131-0
- 1293 Schenzinger, V., Osprey, S., Gray, L., & Butchart, N. (2017). Defining metrics of the
1294 Quasi-Biennial Oscillation in global climate models. *Geoscientific Model Devel-*
1295 *opment*, *10*(6), 2157–2168. doi: 10.5194/gmd-10-2157-2017
- 1296 Schirber, S., Manzini, E., Krismer, T., & Giorgetta, M. (2015). The quasi-
1297 biennial oscillation in a warmer climate: sensitivity to different gravity
1298 wave parameterizations. *Climate Dynamics*, *45*(3-4), 825–836. doi:
1299 10.1007/s00382-014-2314-2
- 1300 Simmons, A., Soci, C., Nicolas, J., Bell, B., Berrisford, P., Dragani, R., ... Schepers,
1301 D. (2020). Global stratospheric temperature bias and other stratospheric
1302 aspects of ERA5 and ERA5.1. *ECMWF Technical Memoranda*, *859*. doi:
1303 10.21957/rcxqfmg0
- 1304 Skamarock, W. C., Snyder, C., Klemp, J. B., & Park, S.-H. (2019). Vertical Res-
1305 olution Requirements in Atmospheric Simulation. *Monthly Weather Review*,
1306 *147*(7), 2641–2656. doi: 10.1175/MWR-D-19-0043.1
- 1307 SPARC. (2022). *SPARC Reanalysis Intercomparison Project (S-RIP) Final Re-*
1308 *port*. M. Fujiwara, G. Manney, L. Gray, and J. Wright (Eds.), SPARC Report
1309 No. 10, WCRP-6/2021. doi: 10.17874/800DEE57D13
- 1310 Stephan, C. C., Strube, C., Klocke, D., Ern, M., Hoffmann, L., Preusse, P., &
1311 Schmidt, H. (2019). Gravity Waves in Global High-Resolution Simulations
1312 With Explicit and Parameterized Convection. *Journal of Geophysical Re-*
1313 *search: Atmospheres*, *124*(8), 4446–4459. doi: 10.1029/2018jd030073
- 1314 Stevens, B., Satoh, M., Auger, L., Biercamp, J., Bretherton, C. S., Chen, X., ...
1315 Zhou, L. (2019). DYAMOND: the DYNAMICS of the Atmospheric general circula-
1316 tion Modeled On Non-hydrostatic Domains. *Progress in Earth and Planetary*
1317 *Science*, *6*(61). doi: 10.1186/s40645-019-0304-z
- 1318 Straub, K. H., Haertel, P. T., & Kiladis, G. N. (2010). An Analysis of Convectively
1319 Coupled Kelvin Waves in 20 WCRP CMIP3 Global Coupled Climate Models.
1320 *Journal of Climate*, *23*(11), 3031–3056. doi: 10.1175/2009JCLI3422.1
- 1321 Takasuka, D., Kodama, C., Suematsu, T., Ohno, T., Yamada, Y., Seiki, T., ... Ma-
1322 sunaga, R. (2024). How Can We Improve the Seamless Representation of
1323 Climatological Statistics and Weather Toward Reliable Global K-Scale Cli-
1324 mate Simulations? *Journal of Advances in Modeling Earth Systems*, *16*(2),

- 1325 e2023MS003701. doi: <https://doi.org/10.1029/2023MS003701>
1326 Tomassini, L., Willett, M., Sellar, A., Lock, A., Walters, D., Whittall, M., . . . Senior,
1327 C. A. (2023). Confronting the Convective Gray Zone in the Global Configura-
1328 tion of the Met Office Unified Model. *Journal of Advances in Modeling Earth*
1329 *Systems*, 15(5), e2022MS003418. doi: 10.1029/2022MS003418
1330 Wheeler, M., & Kiladis, G. N. (1999). Convectively Coupled Equatorial Waves:
1331 Analysis of Clouds and Temperature in the Wavenumber–Frequency Do-
1332 main. *Journal of the Atmospheric Sciences*, 56(3), 374–399. doi: 10.1175/
1333 1520-0469(1999)056<0374:CCEWAO>2.0.CO;2
1334 Yao, W., & Jablonowski, C. (2013). Spontaneous QBO-like oscillations in an at-
1335 mospheric model dynamical core. *Geophysical Research Letters*, 40(14), 3772–
1336 3776. doi: 10.1002/grl.50723
1337 Yao, W., & Jablonowski, C. (2015). Idealized Quasi-Biennial Oscillations in an En-
1338 semble of Dry GCM Dynamical Cores. *Journal of the Atmospheric Sciences*,
1339 72(6), 2201–2226. doi: 10.1175/JAS-D-14-0236.1
1340 Zängl, G., Reinert, D., Rípodas, P., & Baldauf, M. (2015). The ICON (ICOsahedral
1341 Non-hydrostatic) modelling framework of DWD and MPI-M: Description of
1342 the non-hydrostatic dynamical core. *Quarterly Journal of the Royal Meteorolo-*
1343 *gical Society*, 141(687), 563–579. doi: 10.1002/qj.2378